DISSERTATION

STRESS, STRUCTURE, AND FUNCTION OF THE EMBRYONIC HEART

Submitted by
Alex L. Gendernalik
School of Biomedical Engineering

In partial fulfillment of the requirements
For the Degree of Doctor of Philosophy
Colorado State University
Fort Collins, Colorado
Spring 2023

Doctoral Committee:

Advisor: David Bark

Deborah Garrity
Christian Puttlitz
Paul Heyliger

ABSTRACT

STRESS, STRUCTURE, AND FUNCTION OF THE EMBRYONIC HEART

Embryonic heart development is a complex process that requires the coordination of hemodynamic stress and tissue morphogenesis. Improperly timed or distorted mechanical cues can cause reverberating malformations that result in congenital heart defects (CHDs) or embryo death. CHDs occur in $\sim$1% of live births. Only $\sim$20% have a known genetic origin. Altered mechanical signaling or hemodynamics is likely a common contributor to CHD prevalence. Significant research using animal models has shown that altered hemodynamics causes varied malformations. Mechanical properties describe the underlying tissue architecture, which dictates how the heart transmits and reacts to stress. This work aims to quantify and map the mechanical properties to understand how they direct the formation of specific heart structures and function. Furthermore, we seek to understand how mechanical properties change in response to altered hemodynamics. We hypothesize that mechanical properties indicate regions of eventual structure formation, are sensitive to altered hemodynamics, and dictate the pumping method that the heart uses to drive blood flow. We test this hypothesis through three aims. In aim 1, we describe a novel technique in which we use controlled pressurization to deform the embryonic zebrafish heart. We measure deformation in two-dimensions and identify constitutive models of the embryonic heart tissue. Finite element analysis is used to validate our findings in three dimensions. In this aim, we establish that controlled pressurization is a valid technique for inducing measured deformation of the heart. Through this, we determine that the zebrafish myocardial stiffness is on the order of 10 kPa. In aim 2, we further develop our pressurization technique by measuring deformation in three dimensions using confocal microscopy. Furthermore, we use a morpholino antisense oligonucleotide (MO), *gata1*, to alter embryonic zebrafish heart hemodynamics by blocking development of red blood cells, thus decreasing the viscosity and arterial pressure based on Poiseuille's law. Upon mapping strain in three dimensions, we find that strain throughout the heart is variable, with specific regions of low and high strain from 2 to 3 days post-fertilization (dpf). Low arterial pressure in *gata1* MO embryos resulted in significantly increased strain compared to controls, indicating that altered hemodynamics cause altered mechanical properties in the developing embryonic heart. In aim 3, we seek to determine if the zebrafish early embryonic heart tube drives blood flow through peristalsis or impedance-type pumping. We attempt to directly induce impedance pumping by cannulating the atrial inlet of the heart tube after halting contractions and applying a controlled pressure pulse. Additionally, we use precisely controlled temperatures to increase heart rate, thus increasing arterial pressure. As temperature is increased, we use high speed imaging to analyze the contractile motion and resulting blood flow in the tube heart. Furthermore, we describe a previously unknown response whereby the traveling endocardial closure shortens with increased arterial pressure. In this aim, we fail to find evidence of impedance-type pumping but cannot preclude it contributes to blood flow. In summary, our pressurization technique can be used to map strain in the zebrafish embryonic heart; altering hemodynamics by reducing arterial pressure results in decreased stiffness of the embryonic heart myocardium, and endocardial closure length in the embryonic zebrafish heart tube shortens as arterial pressure and heart rate increase.

ACKNOWLEDGEMENTS

This work was made possible by Dr. David Bark's constant support and guidance. He was integral in providing meaning and excitement under extraordinary circumstances. Additionally, through his lessons, I developed an engineer's acumen and abilities. He instilled in me and my colleagues the notion that nearly nothing was beyond our capability. I will carry that mindset with me through life's problems.

Furthermore, I would like to thank Dr. Deborah Garrity and her students, who helped me navigate the world of embryonic zebrafish biology. Here, I developed a researcher's mindset and learned how to investigate the underlying biological mechanisms that influence embryonic development. Thank you for instilling in me the confidence needed to design and undertake experiments with living creatures.

I want to express heartfelt thanks for the ongoing support from Dr. Christian Puttlitz and Dr. Paul Heyliger, who helped me to understand the mechanical engineering concepts I needed to approach my work on embryonic zebrafish hearts. Notably, during our discussions, they pointed out the importance and uniqueness of my work. I will always draw motivation from the suggestions and kindness of my committee members.

Finally, my parents were unwavering in their support of my education. They never had a negative sentiment and always encouraged me to continue through difficult times. From an early age, my dad, Larry Gendernalik, taught me never to fear a problem and that the solution will come with careful thought and exploration. Here is where I developed the underlying mechanism of an engineer. My mother, Larisa Gendernalik, instilled in me the persistence of an athlete. Her smile and humor helped me out of the deepest of ruts. My memory of my sister, Valerie Gendernalik, gave me the final push I needed when faced with exceptional difficulties. My friends provided me with endless laughs and the excitement of adventures to come. My gratitude toward my family and friends is infinite and indescribable.

TABLE OF CONTENTS

ABSTRACT ii
ACKNOWLEDGEMENTS iv
LIST OF TABLES vii
LIST OF FIGURES viii

Chapter 1 Background 1
  1.1 Congenital Heart Defects 1
  1.2 Animal Studies 2
  1.3 Embryonic Heart Development 4
  1.4 Hemodynamic Stresses 5
  1.5 Mechanical Properties 6
  References 7

Chapter 2 Aim 1: Passive Mechanical Properties of the Embryonic Heart Resemble Single Myocytes 12
  2.1 Introduction 12
  2.2 Methods 13
    2.2.1 Zebrafish Embryo Preparation 13
    2.2.2 Two-Dimensional Imaging 14
    2.2.3 Cannulation and Pressurization 14
    2.2.4 Constitutive Model 15
    2.2.5 Two-Dimensional Model Approximation of Mechanical Properties Assuming a Thin-Walled Pressure Vessel 17
    2.2.6 Two-Dimensional Parameter Estimation 18
    2.2.7 2D Image and data Analysis for the 2D Approximation of Mechanical Properties Assuming a Thin-Walled Pressure Vessel 19
    2.2.8 Three-Dimensional Imaging 20
    2.2.9 Finite Element Analysis 20
  2.3 Results 21
    2.3.1 Mechanical Response of Atrium to Pressure Loading 21
    2.3.2 Mechanical Properties and Parameter Estimation 21
    2.3.3 Finite Element Analysis 22
  2.4 Discussion 25
  References 29

Chapter 3 Aim 2: 3D Patterns of Strain Depend on Specific Hemodynamic Cues 35
  3.1 Introduction 35
  3.2 Methods 36
    3.2.1 Zebrafish Embryo Preparation 36
    3.2.2 *Gata1* Knockdown by Morpholino 36
    3.2.3 Cannula preparation 37

3.2.4 Embryo orientation and mounting 38
3.2.5 Cannulation 39
3.2.6 Pressurization and Imaging 40
3.2.7 Image processing and Deformation Analysis 40
3.2.8 Regional Strain and Cell Density Analysis 41
3.3 Results 42
3.3.1 Ventricular and Atrial Expansion Upon Pressure Loading 42
3.3.2 Strain Mapping and Regional Analysis 44
3.4 Discussion 48
References 50

Chapter 4 Aim 3: Early Heart Pumping Behavior 53
4.1 Introduction 53
4.2 Methods 54
4.2.1 Zebrafish Preparation and Imaging 54
4.2.2 Red Blood cell and Closure Tracking 54
4.2.3 Impedance Pulsing 55
4.3 Results 57
4.4 Discussion 60
References 61

Chapter 5 General Conclusions and Future Directions 64
References 67

LIST OF TABLES

2.1 Coefficients generated from experimental model fits of Eq. (2.1) (Neo-Hookean), Eq. (2.2) (reduced polynomial), and Eq. (2.3) (exponential). 25

3.1 Pressurization sequence. 41

LIST OF FIGURES

1.1 Early embryonic heart pumping sequence. 6

2.1 2D pressurization stretch directions (a), needle location (b), experimental hardware setup (c), 48 hpf zabrafish heart 3D confocal image (d), and FEA strain measurement locations (e). 16
2.2 2D image of heart before pressurization (a). 2D image of heart after pressurization (b). Plot of pressure vs. normalized area (c). 22
2.3 Plot of Green strain in the axial direction (E_{ZZ}) vs in the circumferential direction ($E_{\theta\theta}$). 23
2.4 Plots of pressure (mmHg) vs. circumferential and longitudinal stretch (λ_{zz} and $\lambda_{\theta\theta}$) for each embryo. Line indicates Hookean model fit. 23
2.5 Plots of pressure (mmHg) vs. circumferential and longitudinal stretch (λ_{zz} and $\lambda_{\theta\theta}$) for each embryo. Line indicates Single Cell model fit. 24
2.6 Plots of pressure (mmHg) vs. circumferential and longitudinal stretch (λ_{zz} and $\lambda_{\theta\theta}$) for each embryo. Line indicates Eq. (2.3) model fit. 24
2.7 Plot of Pressure (mmHg) vs. maximum stretch ratios for experimental data, Reduced Polynomial simulation data, and Neo-Hookean simulation data. 26
2.8 Three-dimensional max principal logarithmic strain map of a simulated 48 hpf zebrafish heart pressurized to 2 mmHg using a Neo-Hookean and Reduced Polynomial model. 26

3.1 Beveled cannula tip. 37
3.2 Point cloud and region definitions generated from the 3D geometry of an embryonic zebrafish heart. 42
3.3 2-dpf ventricle and atrium pressure vs. stretch plot 43
3.4 3-dpf ventricle and atrium pressure vs. stretch plot 43
3.5 *Gata1* MO treated 3-dpf ventricle and atrium pressure vs. stretch plot 44
3.6 Regional max strains (eigen values) and cell-to-cell distances for 2 and 3-dpf hearts. . . 45
3.7 2-dpf (embryo 1) max strain (eigen value) map for a pressurized embryonic zebrafish heart 45
3.8 2-dpf (embryo 2) max strain (eigen value) map for a pressurized embryonic zebrafish heart 46
3.9 3-dpf (embryo 1) max strain (eigen value) map for a pressurized embryonic zebrafish heart 46
3.10 3-dpf (embryo 2) max strain (eigen value) map for a pressurized embryonic zebrafish heart 46
3.11 Atrioventricular junction max strain (eigen value) for 2 and 3-dpf embryonic zebrafish hearts 47
3.12 Atrioventricular junction max strain (eigen value) for 3-dpf and 3-dpf, *gata1* MO treated embryonic zebrafish hearts 47
3.13 *Gata1* MO treated 3-dpf (embryo 1) max strain (eigen value) map for a pressurized embryonic zebrafish heart 48

3.14 *Gata1* MO treated 3-dpf (embryo 2) max strain (eigen value) map for a pressurized embryonic zebrafish heart 48
3.15 Atrioventricular junction max strain (eigen value) for 3-dpf and 3-dpf, *gata1* MO treated embryonic zebrafish hearts 48

4.1 24 hour post-fertilization zebrafish heart closure definitions 55
4.2 24 hour post-fertilization zebrafish and tube heart image. 56
4.3 Applied pressure pulse parameters. 56
4.4 Plot of heart rate vs. temperature for 24 hpf zebrafish hearts (a). Plot of max RBC velocity vs. heart rate (b). Plot of closure length vs. heart rate for 24 hpf zebrafish hearts (c). 57
4.5 Plot of inlet RBC and trailing-edge flow rate over one cycle (a). Plot of outlet RBC and leading-edge flow rate over one cycle (b). 58
4.6 Correlation plots of max leading and trailing-edge velocities vs. max inlet and outlet RBC velocities. 59

Chapter 1

Background

1.1 Congenital Heart Defects

Congenital heart defects (CHDs) affect 1% of newborns, often with devastating consequences [1]. However, the causes are poorly understood and only 20% have a known genetic etiology. Altered mechanical signaling or mechanotransduction may be one key contributor. The mechanical environment is spatially and temporally dynamic as the heart begins to function before it is fully formed through a complex coordination of processes. Throughout development, 'normal' mechanical feedback from the hemodynamic environment is required for cardiac cells as they mature, migrate, and proliferate. Any abnormal mechanical signaling early in development may reverberate to cause compounding defects in the subsequent formation of heart structures such as the chambers, valves, or trabeculae.

Due to their complex origin and a wide diversity in defect phenotype, CHDs range significantly in form and severity. CHDs are often classified based on similarities of the affected anatomical area and severity [2]. Mild CHDs include atrial and ventricular septal defects and patent ductus arteriosus. Mild CHDs comprised 57.9% of cases, with ventricular septal defects having the highest prevalence of all CHDs (35.6%) [3]. Often, mild CHDs resolve spontaneously or require minimal intervention compared to severe CHDs. Severe CHDs are characterized by functional defects resulting in low blood oxygenation (cyanotic defects), including underdeveloped structures or defective valves.

In some cases, the aortic valve may fail to function properly, resulting in valve stenosis and low blood flow out of the left ventricle. Restricted blood flow can result in abnormally high pressure in the ventricle. Aortic stenosis occurs when the aortic valve is thickened and immobile and is evident from turbulent or decreased Doppler flow. Corrective treatment is done through *in utero* aortic valvuloplasty, in which a balloon is placed over the stenosed aortic valve and inflated, forcing the valve opening to enlarge. Subsequently, flow in the aorta increases and the high ventricular pressure is relieved. If aortic stenosis is not corrected, and abnormal hemodynamic forces are allowed to persist, more serious congenital heart defects may arise.

Hypoplastic left heart syndrome (HLHS) results from heart remodeling due to low flow caused by a dysfunctional aortic valve. Phenotypic characteristics of HLHS include arrested growth or hyperplasia of the left ventricle and narrowed aorta. In normal fetal hearts, the foramen ovale and ductus arteriosus are open, allowing blood to flow freely between the left and right atria and from the pulmonary artery to the aorta, respectively. These pathways close before birth. However, in HLHS-affected hearts, the underdeveloped left ventricle cannot adequately pump blood to the body. As such, doctors may choose to keep the pathways open with medication, thus allowing the right side of the heart to provide blood flow to the entire body, bypassing the defective left ventricle. However, only a fraction of the blood will be oxygenated, and eventually, the right side of the heart will not be able to supply the growing body. Surgical correction of HLHS is a staged, reconstructive process that can last into three years of age. The final outcome is called "Fontan circulation" and involves rerouted blood circulation to the lungs and a single functioning ventricle [4]. However, patients will live with lifelong complications such as arrhythmia, higher risk for Protein Losing Enteropathy, and thromboembolism [5–7]. Although the survival rate for surgically corrected HLHS cases has continuously improved, fetal aortic valvuloplasty improves survivability to six years old by 25% [8]. Fetal aortic valvuloplasty to prevent progression to HLHS is an example of the manipulation of hemodynamics to treat disease. It is evidence that blood flow mechanics directly affect heart development. By understanding the flow environment and the biomechanical response of the cells comprising the heart tissue, further prevention of CHDs may become possible.

1.2 Animal Studies

Many animal studies have been conducted that use alterations to flow or structure as a means to investigate growth and remodeling of the embryonic heart. The most common animal models used are mouse, chick, and zebrafish. This has been done through various avenues including genetic manipulations (i.e., knockdowns), pharmacological treatments, and surgical interventions. Midgett et al. used a surgical technique to manipulate blood flow through the heart [9, 10]. In chicks, a suture was tied around the outflow tract during the heart tube stage and tightened to constrict the tract by 10-35% or 35-60%. Sutures were left on for $\leq$1 day. Less constriction resulted in more minor ventricular septal defects, whereas greater constriction caused double-outlet right ventricle, thus demonstrating the potential for CHD severity to be regulated by flow in a dose-dependent manner. In a different study by Hove et al., a glass bead was implanted at the inflow or outflow tracts of an embryonic zebrafish heart, resulting in impaired valve formation, a lack of looping, and collapsed or fused-shut inflow and outflow tracts. While the latter two conditions would clearly be quite severe in humans, some level of impaired valve formation is thought to occur in 40% of CHDs [11]. These experiments highlight the sensitivity of the developing heart to pressure and flow alterations, which is highly relevant when considering the potential changes in fetal cardiovascular biomechanics as a consequence of increased maternal risk factors due to drug use or blood flow-altering treatments.

The effects of altered hemodynamics on valvulogenesis is particularly well studied due to diverse mechanical signaling in the atrioventricular junction (AVJ). The constricted geometry results in higher blood flow velocity and wall shear stress than in the chambers [12, 13]. Furthermore, the AVJ is located between two sequentially contracting chambers; thus, reverse or oscillatory flows can occur depending on the pressure difference across the AVJ. Bartman et al. used a transgenic zebrafish line in which cardiac troponin T (*tnnt2*) is not produced, thus preventing the heart from contracting [14]. In this case, the endocardial cushions (heart valve precursors) failed to form at the AVJ. To determine which mechanical cue, myocardial function (contraction) or endothelial shear stress, determines endothelial cushion development, a different line called *cardiofunk* (*cfk*) was used. In this line, contraction still occurs, but circulation is stopped due to cardiac dilation resulting from defects in sarcomeric actin polymerization (R177H mutation), which results in lower, but not zero, contractile force [15]. They observed that the endocardial cushions failed to form in 50% of *cardiofunk* embryos. Furthermore, when contraction was reduced by administering the pharmaceutical 2,3-Butanedione monoxime (BDM), a dose-dependent response in endocardial cushion formation was observed. Bartman et al. conclude that myocardial function is primarily responsible for endocardial cushion formation from these experiments. However, flow through the AVJ was not reduced to zero; thus, the endothelial cells were still exposed to wall shear stress. These experiments highlight the difficulty in decoupling biomechanical signals (i.e., contraction, wall shear stress, and pressure).

Vermot et al. hypothesized that reversing blood flows at the AVJ provides the primary signals needed for proper valvulogenesis [13]. Reversing blood flow is quantified as retrograde flow fraction (RFF), the fraction of the cardiac cycle during which retrograde/reverse flow occurs. To investigate the RFF signal, a type of genetic knockdown called an antisense morpholino oligonucleotide (MO) was used to block transcription of *gata1*, a gene that regulates erythropoiesis. As a result, the blood did not contain any circulating red blood cells, which caused a 90% reduction in viscosity. Notably, RFF through the AVJ was greater than in controls (45% RFF in *gata1* morphants vs. 35% in control embryos). Blocking of *gata2*, also a regulator of erythropoiesis, resulted in a 72% reduction of red blood cells, a 70% reduction in viscosity, and significantly reduced RFF (17% *gata2* morphants vs. 35% in control embryos). The authors found that the *gata1* embryos had normally developed valves while the *gata2* embryos had severely defective valves. In a combined *gata1* and *gata2* MO knockdown experiment, the resulting RFF was 50%, and valve formation was again normal. Based on this, the authors conclude that reversing flows are more critical for valve development than shear stress magnitude alone.

1.3 Embryonic Heart Development

In In the heart's earliest functional form, it is a straight tube that is made up of 3 distinct layers: an inner blood-contacting cellular monolayer of endocardial cells, a middle viscous gel-like layer called the cardiac jelly, and an outer contractile monolayer of cardiomyocytes. This early heart tube seems to pump in a peristaltic-like manner, in that sequential contraction of the myocardial cells results in a blood volume-displacing wave [16, 17]. Although active pumping is occurring, red blood cells have yet to develop, and substantial morphogenesis will transpire before the final form. It has been suggested that the heart might function purely to support its own morphological development in these early stages [14]. Shortly after newly formed red blood cells begin circulating, the heart tube undergoes "looping," A series of bending and twisting actions that result in an S-shaped tube [18]. Following looping is chamber ballooning and the formation of the atrium and ventricle. Next, the trabeculae and valves begin to form. In trabeculation, cardiomyocytes in the ventricular myocardium migrate toward the ventricle lumen. As the trabecular volume increases, so does the contractility and, thus, blood flow. Valvulogenesis occurs at the AVJ, where a constriction or endothelial ring separates the two chambers. This process begins with an accumulation of cardiac jelly and endocardial cells at the constriction, followed by more endocardial cells migrating to form the leaflets [14]. The final basic form of the zebrafish heart consists of two sequentially contracting chambers with a valve in between to prevent reverse flow.

1.4 Hemodynamic Stresses

Contraction and blood flow through the embryonic heart cause several types of stress in the heart tissue. This stress varies throughout a single heart cycle or when downstream hemodynamics conditions change. During the early heart tube stages, contraction begins near the inlet. Contraction increases pressure, driving blood flow forward (Figure 1.1). This flow creates wall shear stress, which depends on the blood viscosity and blood velocity gradient [19]. As the contractile wave travels forward, pressure increases on the arterial side due to resistance imparted by the vasculature. Pressure increases result in circumferential stress, a type of intercellular stress that is transmitted through cell-cell adhesion. With increased blood viscosity, resistance increases proportionally per the Poiseuille law [20]. This results in an increase in pressure and, thus, circumferential stress. Traction stress occurs between the cells and extracellular matrix (ECM) through cell-ECM integrin adhesion molecules. Overall, stress increases greatly during contraction, specifically at the end of systole (ejection) when the heart is pumping against the highest pressure.

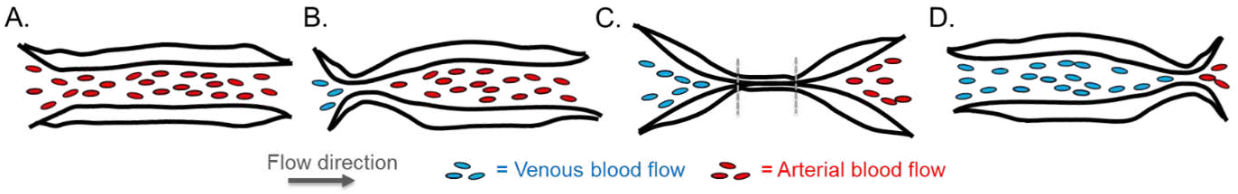

Figure 1.1: Illustration of blood volume changes during one cycle. A) Volume of heart tube is not changing with time. B) Atrial inlet closes. C) Venous volume increases, arterial volume decreases, dashed lines indicate endothelial closure with trailing edge on left and leading edge on right. D) Closure reaches outlet, arterial volume is zero.

1.5 Mechanical Properties

Stress in the embryonic heart is complex. Contraction and hemodynamics create time-varying stress that is transmitted or dampened by various components of the cells and ECM that make up the heart walls. The mechanical properties of the heart describe how the tissue deforms in response to stress. Cytoskeletal components, such as myosin and actin filaments, and ECM components, such as fibronectin, contribute to the overall mechanical properties. Furthermore, actin or other filamentous components may align in specific prevailing directions. In such cases, the material properties may be defined as transversely isotropic, where material behavior differs in the fiber vs. non-fiber directions. Importantly, the material properties can be measured and, when appropriately modeled, can accurately describe how the heart tissue will deform.

Measuring the material properties of the embryonic heart presents several problems. Firstly, it is an embedded organ that is tightly connected to the surrounding tissue. Thus, removal may alter how stress is conveyed, particularly if the tissue is damaged. With that, most measurement techniques are invasive and inevitably require sacrifice of the embryo. As such, an appropriate animal model must be used. Secondly, the embryonic heart in most standard animal models is relatively small. Many common measurement techniques, such as uniaxial or biaxial testing, are not feasible. These techniques require the removal of the tissue to be placed in a machine that pulls the tissue in the desired direction. Deformation of the tissue is measured, and based on the force applied, a relationship between force and deformation can be created to develop an appropriate material model. Fortunately, small-scale techniques that produce the same outcomes have been developed.

Micro or tissue indentation is a scalable material property measurement technique. Other similar types of indentation include Atomic Force Measurement and cell pokers, which use a force transducer to measure the force generated by pressing on the tissue [21, 22]. The amount of deflection by the probe is also measured. From this, a relationship between force and deflection is ascertained. Length scales for these systems range from nanometer fractions to centimeters. Tissue indentation has been used to characterize the material properties of embryonic chick hearts, allowing researchers to probe specific heart regions [23–25]. Indentation techniques can be relatively non-invasive since they only require the probe to contact the tissue surface. However, they are limited in that they can only be used to measure compressive forces, not tensile forces [23]. Tensile strength allows the cells and tissue to resist being stretched or pulled and is mostly contained within the cytoskeleton and extracellular matrix. Filamentous components of cardiomyocytes, particularly sarcomeric actin but also including non-sarcomeric cytoskeletal components (actin, intermediate filaments, and microtubules), transmit and resist tensile forces from circumferential stress [26]. Pressure loading is advantageous for measuring mechanical properties in organs undergoing circumferential stress. In this technique, a tube or cannula is inserted into a vessel, and controlled pressure is applied to inflate the vessel [27, 28]. The embryonic heart tissue is under constant and cyclic stress from internal pressure and contraction. Given this, measuring mechanical properties by applying force from within the chambers will likely provide properties that describe the tissue behavior under physiologic conditions. Overall, the appropriate method should be chosen based on the forces involved (i.e., compression or tension).

References

[1] Julien I E Hoffman and Samuel Kaplan. The incidence of congenital heart disease. *Journal of the American college of cardiology*, 39(12):1890–1900, 2002.

[2] Yingjuan Liu, Sen Chen, Liesl Zühlke, Graeme C Black, Mun-kit Choy, Ningxiu Li, and

Bernard D Keavney. Global birth prevalence of congenital heart defects 1970–2017: updated systematic review and meta-analysis of 260 studies. *International Journal of Epidemiology*, 48(2):455–463, 02 2019.

[3] Lorenzo D Botto, Angela E Lin, Tiffany Riehle-Colarusso, Sadia Malik, and Adolfo Correa. Seeking causes: classifying and evaluating congenital heart defects in etiologic studies. *Birth Defects Research Part A: Clinical and Molecular Teratology*, 79(10):714–727, 2007.

[4] William I Norwood Jr, Marshall L Jacobs, and John D Murphy. Fontan procedure for hypoplastic left heart syndrome. *The Annals of thoracic surgery*, 54(6):1025–1030, 1992.

[5] Alyssa M Bernardi, Sylvestor Moses, Brent J Barber, Marlys H Witte, and Michael D Seckeler. Higher Incidence of Protein-Losing Enteropathy in Patients with Single Systemic Right Ventricle. *Pediatric cardiology*, 42(1):178–181, jan 2021.

[6] Yoshimichi Kosaka, Takahiko Sakamoto, Kiyohiro Takigiku, Satoshi Yasukochi, and Yorikazu Harada. Coronary thromboembolism in hypoplastic left heart syndrome. *The Annals of thoracic surgery*, 95(2):718, feb 2013.

[7] Annemien E van den Bosch, Jolien W Roos-Hesselink, Ron Van Domburg, Ad JJC Bogers, Maarten L Simoons, and Folkert J Meijboom. Long-term outcome and quality of life in adult patients after the fontan operation. *The American journal of cardiology*, 93(9):1141–1145, 2004.

[8] Sarah S Pickard, John B Wong, Emily M Bucholz, Jane W Newburger, Wayne Tworetzky, Terra Lafranchi, Carol B Benson, Louise E Wilkins-Haug, Diego Porras, Ryan Callahan, et al. Fetal aortic valvuloplasty for evolving hypoplastic left heart syndrome: a decision analysis. *Circulation: Cardiovascular Quality and Outcomes*, 13(4):e006127, 2020.

[9] Madeline Midgett, Sevan Goenezen, and Sandra Rugonyi. Blood flow dynamics reflect degree of outflow tract banding in Hamburger-Hamilton stage 18 chicken embryos. *Journal of the Royal Society, Interface*, 11(100):20140643, nov 2014.

[10] Madeline Midgett and Sandra Rugonyi. Congenital heart malformations induced by hemodynamic altering surgical interventions. *Frontiers in physiology*, 5:287, aug 2014.

[11] Jay R Hove, Reinhard W Köster, Arian S Forouhar, Gabriel Acevedo-Bolton, Scott E Fraser, and Morteza Gharib. Intracardiac fluid forces are an essential epigenetic factor for embryonic cardiogenesis. *Nature*, 421(6919):172–177, 2003.

[12] Emilie Heckel, Francesco Boselli, Stéphane Roth, Alice Krudewig, Heinz-Georg Belting, Gilles Charvin, and Julien Vermot. Oscillatory flow modulates mechanosensitive klf2a expression through trpv4 and trpp2 during heart valve development. *Current biology*, 25(10):1354–1361, 2015.

[13] Julien Vermot, Arian S Forouhar, Michael Liebling, David Wu, Diane Plummer, Morteza Gharib, and Scott E Fraser. Reversing blood flows act through klf2a to ensure normal valvulogenesis in the developing heart. *PLoS biology*, 7(11):e1000246, 2009.

[14] Thomas Bartman, Emily C Walsh, Kuo-Kuang Wen, Melissa McKane, Jihui Ren, Jonathan Alexander, Peter A Rubenstein, Didier Y R Stainier, and Brigid Hogan. Early myocardial function affects endocardial cushion development in zebrafish. *PLoS biology*, 2(5):e129, 2004.

[15] Kuo-Kuang Wen and Peter A Rubenstein. Biochemical consequences of the cardiofunk (r177h) mutation in yeast actin. *Journal of Biological Chemistry*, 278(48):48386–48394, 2003.

[16] Mark C Fishman and Kenneth R Chien. Fashioning the vertebrate heart: earliest embryonic decisions. *Development*, 124(11):2099–2117, 1997.

[17] Antoon F M Moorman, Alexandre T Soufan, Jaco Hagoort, Piet A J de Boer, and Vincent M Christoffels. Development of the building plan of the heart. *Annals of the New York Academy of Sciences*, 1015(1):171–181, 2004.

[18] Larry A Taber. Biophysical mechanisms of cardiac looping. *International Journal of Developmental Biology*, 50(2-3):323–332, 2003.

[19] R Aidan Jamison, Chaminda R Samarage, Robert J Bryson-Richardson, and Andreas Fouras. In vivo wall shear measurements within the developing zebrafish heart. *PloS one*, 8(10):e75722, 2013.

[20] Juhyun Lee, Tzu-Chieh Chou, Dongyang Kang, Hanul Kang, Junjie Chen, Kyung In Baek, Wei Wang, Yichen Ding, Dino Di Carlo, Yu-Chong Tai, et al. A rapid capillary-pressure driven micro-channel to demonstrate newtonian fluid behavior of zebrafish blood at high shear rates. *Scientific reports*, 7(1):1980, 2017.

[21] A Emad, William F Heinz, Matthew D Antonik, Neill P D'Costa, Soni Nageswaran, Cora-Ann Schoenenberger, Jan H Hoh, et al. Relative microelastic mapping of living cells by atomic force microscopy. *Biophysical journal*, 74(3):1564–1578, 1998.

[22] BILL Daily, Elliot L Elson, and GEORGE IRENEUS Zahalak. Cell poking. determination of the elastic area compressibility modulus of the erythrocyte membrane. *Biophysical journal*, 45(4):671–682, 1984.

[23] Evan A Zamir, Varahoor Srinivasan, Renato Perucchio, and Larry A Taber. Mechanical asymmetry in the embryonic chick heart during looping. *Annals of biomedical engineering*, 31(11):1327–1336, dec 2003.

[24] E A Zamir and L A Taber. Material properties and residual stress in the stage 12 chick heart during cardiac looping. *J. Biomech. Eng.*, 126, 2004.

[25] E A Zamir and L A Taber. On the effects of residual stress in microindentation tests of soft tissue structures. *J. Biomech. Eng.*, 126, 2004.

[26] Kelly M Grimes, Vikram Prasad, and James W McNamara. Supporting the heart: Functions of the cardiomyocyte's non-sarcomeric cytoskeleton. *Journal of molecular and cellular cardiology*, 131:187–196, 2019.

[27] P Ling, LA Taber, and JD Humphrey. Approach to quantify the mechanical behavior of the intact embryonic chick heart. *Annals of Biomedical Engineering*, 30:636–645, 2002.

[28] Alex Gendernalik, Banafsheh Zebhi, Neha Ahuja, Deborah Garrity, and David Bark. In vivo pressurization of the zebrafish embryonic heart as a tool to characterize tissue properties during development. *Annals of biomedical engineering*, 49(2):834–845, 2021.

Chapter 2

Aim 1: Passive Mechanical Properties of the Embryonic Heart Resemble Single Myocytes

2.1 Introduction

Morphological sculpting during cardiogenesis involves a complex interplay between tissue growth, mechanical properties, and function [1]. This interplay is fundamental to modeling and remodeling of tissue as the afterload on the heart increases in response to the growing demands of the body [2–7]. When encountering abnormal mechanical stress, the adaptive responses can lead to morphology reminiscent of congenital heart defects [8, 9]. To better understand the relationships in both health and disease, it is first necessary to develop approaches to quantify mechanical properties in animal models used to study heart development.

Just after looping, the embryonic heart is composed of three layers and two chambers (atrium and ventricle). The endocardium and cardiac jelly (CJ) are the innermost layers that provide little to no tensile support [10–12]. The outer myocardium is composed of a single sheet of contractile cardiomyocytes at the early embryonic heart stages, providing much of the tensile support [12]. Passive tensile support primarily comes in the form of intracellular filamentous actin, while active support exists through interconnected sarcomeres [13, 14]. The development and coordination of each layer with their corresponding mechanical properties results in a functional heart.

Quantifying mechanical properties can be done through uniaxial or biaxial tissue testing. The need for a sufficient tissue sample size is a limiting factor for these techniques. Despite this, these tests have been successfully applied to embryonic chick hearts and small lymphatic vessels, which are greater than 200 μm in length scale [15, 16]. Alternatively, on the cellular scale, many other tools exist, including micro-indentation, atomic force microscopy (AFM), cell aspiration, magnetic tweezers, and optical tweezers [17, 18]. When employing these techniques, properties are only locally measured. Furthermore, these approaches do not provide physiological tensile loads, typical of the heart, and are very challenging to use on the scale of a zebrafish embryonic heart chamber (50–200 μm). Therefore, techniques to quantify mechanical properties of embryonic cardiac tissue have seen little application in zebrafish, which otherwise are a useful animal model for studying early heart development due to their optical clarity and extensive library of transgenic lines.

Here we demonstrate a novel pressurization technique to measure passive mechanical properties of the embryonic zebrafish atrium in vivo, building upon what has been done in explanted chick hearts [19, 20]. Although we neglect observations on the ventricle, we note that at these early developmental stages, the atrium provides much of the work required for early circulation [21]. The technique can be applied throughout development and to various genetic zebrafish models, while the zebrafish remains alive. In the current example, we apply the technique at an early developmental stage directly after a morphological transformation known as looping [22]. Constitutive models, based on previously published research, are applied to planar cross-sectional data and these models are evaluated in a three dimensional finite element analysis (FEA). Overall, we present a tool that can be leveraged when identifying phenotypes in zebrafish models, considering the mechanical properties are intimately linked with heart function and morphology.

2.2 Methods

2.2.1 Zebrafish Embryo Preparation

Embryos were obtained from fertilized eggs collected from adult zebrafish (*Danio rerio*), raised and bred in accordance with Westerfield [23]. Ethical approval for experiments was provided by the Institutional Animal Care and Use Committee at Colorado State University. Time of fertilization and developmental age was confirmed by cell counting during the zygote or early cleavage period. Embryos were maintained at 28°C until experimentation. At 48 hours post-fertilization (hpf), embryos were dechorionated and transferred to a solution of 4 μg/mL Warfarin in E3 (balanced salts embryo medium) where they were incubated for approximately 10 min. Warfarin was used to mitigate risk of blood coagulation during cannulation, described below. Embryos were then embedded in 1.5% low-melt agarose to physically immobilize them. 2,3-butanedione monoxime (BDM) was added to the 1.5% agarose solution at a concentration of 50 mM with continuous exposure to maintain an appropriate dosage [24]. BDM is an inhibitor of myosin ATPase, inhibiting cardiomyocyte contraction and is therefore used to stop the heart during measurements [25]. BDM is also commonly used to study passive properties of adult hearts [26]. A 15-min incubation time was sufficient to halt contractions. Note that the zebrafish remain alive during this time and can survive multiple days without blood circulation [27, 28]. A total of six embryos were used in this study, five embryos were used in the two-dimensional pressurization experiments and one representative embryo for three-dimensional imaging.

2.2.2 Two-Dimensional Imaging

Images were acquired at room temperature with an upright microscope (Olympus SZX12 with SZXAL20X lens attachment) by a Photron Fastcam Mini UX-100 camera at .45 μm/pixel with an optical resolution of .88–1.5 μm. Data were collected as image sequences for analysis. Embryos were oriented ventral side up with the atrioventricular canal (AVC) and atrial inlet (AI) in the imaging plane, Figure 2.1a.

2.2.3 Cannulation and Pressurization

Borosilicate glass capillaries (WPI, Sarasota, FL, TW100-6) were pulled and broken to an outer diameter of 10–15 μm, as optically measured. Capillaries were soaked in casein solution overnight to prevent blood-protein binding and blood clotting. An injection solution consisting of 4 μg/mL Wafarin (to further prevent clotting) and .1 mg/mL Rhodamine dye (to visualize potential leakage) in 0.3X Danieau's solution was backfilled into capillaries. Danieau's solution resembles the salt concentrations and osmotic pressures observed within zebrafish embryos [29]. Capillaries were attached to a micromanipulator, where the tip was used to puncture a 50 μm2 area located at the confluence of the cardinal veins, posterior to the atrial inlet, Figure 2.1b. A pressurization system, consisting of a fluid column connected to the cannula via a small tube and a syringe pump (Harvard

Apparatus, Holliston, MA, PHD 2000) by which the fluid level in the column can be precisely controlled, was used to produce specified pressures, Figure 2.1c. All air bubbles were purged and the fluid level in the column was zeroed to the level of the zebrafish heart prior to cannulation, corresponding to a near zero-pressure state. This was determined when fluid did not enter or exit the cannula. Cannulation, itself, did not appear to initiate any response from the heart, despite creating a local injury. This was verified by comparing images of heart size and morphology between cannulated and non-cannulated zebrafish. Note that contractility was stopped with BDM before pressurization began, as described above. Once the capillary was inserted, pressure was increased from 0 to 10 mmHg and image sequences were collected at every 0.5 mmHg increment until 2 mmHg with 60 s intervals between each pressurization, allowing viscoelastic effects to dissipate. Thereafter, imaging was executed at every 2-mmHg increment. 0.5 mmHg increments for physiologic pressure ($\leq$2 mmHg) was chosen to resolve potential nonlinearities [21]. We speculate that pressure is applied throughout the entire cardiovascular system with this technique. Tissue was allowed to stabilize between pressurization steps and there was negligible flow out of the cannula once pressure equilibrium was reached. Also, note that the diameter of the fluid column was large when compared to the zebrafish and therefore any volume changes that occur to expand the cardiovascular system was relatively negligible when compared to the volume of liquid added during pressurization steps. Therefore, hydrostatic pressure changes were negligible. Also dye from the cannulation media did not travel more than a 20 um radius from the cannulation site, indicating only small volume changes.

2.2.4 Constitutive Model

A valid constitutive model for the embryonic zebrafish heart has not been developed before, to our knowledge. We therefore compared three models of increasing complexity to determine the best representation of the embryonic myocardium over a range of applied pressures. As a first order approximation, a Neo-Hookean model was evaluated. The strain energy density function

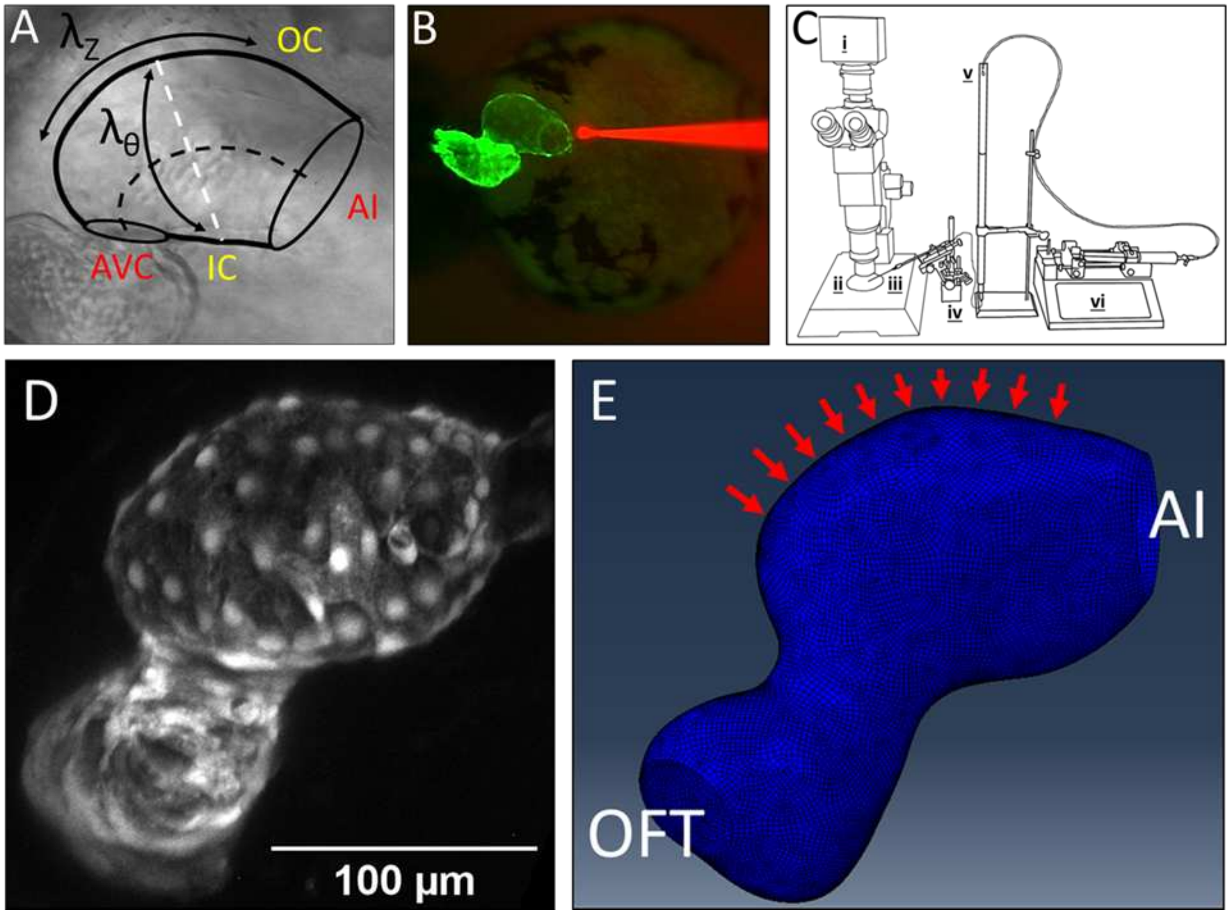

Figure 2.1: (a) Image of the 48 hpf zebrafish heart with outlined atrium. Black dotted center line represents longitudinal length of the atrium. Atrial inlet (AI) and atrioventricular canal (AVC) mark the boundaries and constriction of the atrium. White dotted line indicates half the length of the atrium where radius measurements were taken. Outer curvature (OC) is outlined by upper black line. Inner curvature (IC) is outlined by lower black line. λ_{zz} indicates longitudinal stretch direction relative to the atrium and $\lambda_{\theta\theta}$ indicates circumferential stretch direction. (b) Epifluorescence microscopy image of the *Tg(my17:EGFP)* 48 hpf zebrafish heart with fluorescent myocardium (green) viewed ventrally. This image illustrates the location of cannula (filled with red rhoadamine dye) insertion and pressurization, posterior of the atrial inlet. (c) Illustration of pressurization system consisting of camera (i), petri dish or slide containing live zebrafish (ii), cannula (iii), micromanipulator (iv), fluid column (v), and syringe pump (vi). (d) Laser scanning confocal three dimensional image of a fluorescent 48 hpf zebrafish heart. (e) Zebrafish heart model mesh. Boundary conditions were applied at the ventricle outflow tract (OFT) and the atrial inlet (AI). Red arrows indicate points at which simulated strain measurements were taken.

representing the embryonic myocardium as an incompressible, homogenous material in this case is

$$W = \frac{1}{2}C_H(I_C - 3), \tag{2.1}$$

where C_H is a material constant and I_C is the first strain invariant $I_c = \lambda_{RR}^2 + \lambda_{\theta\theta}^2 + \lambda_{ZZ}^2$, where stretch ratios are defined by $\lambda_{\theta\theta} = \frac{r}{R}$, $\lambda_{zz} = \frac{l}{L}$, $\lambda_{rr} = \frac{\partial r}{\partial R}$, along the circumferential, axial, and radial directions. The term r is the deformed radius, R is the nearly stress free radius, l is the deformed axial length, L is the nearly stress-free axial length, ∂r is the deformed myocardial thickness, and ∂R is the nearly stress-free thickness. As a limitation, we assume no residual stress or twist with these equations. Note that no twist is seen when observing individual cardiomyocytes in zebrafish during pumping or inflation at this stage in development. We also evaluated an isotropic hyperelastic Yeoh-type, or reduced polynomial, strain energy density function that has been previously used to study continuous sheets of cells [30–32]:

$$W = C_S(I_C - 3) + C_{S1}(I_C - 3)^2, \tag{2.2}$$

where C_S and C_{S1} are unknown constants. Lastly, to compare with prior work on chick embryos, we also evaluated an isotropic, incompressible, homogenous, nonlinear model [12]. The strain energy density function in this case is based off of one used for the human carotid bifurcation [33, 34]:

$$W = \frac{C_I}{C_{I1}} \left[\exp\left(\frac{1}{2} C_{I1}(I_C - 3) \right) - 1 \right], \tag{2.3}$$

where C_I and C_{I1} are material-specific constants [12, 35]. Note that models with additional constants could result in overfitting of the data based on our current approach.

2.2.5 Two-Dimensional Model Approximation of Mechanical Properties Assuming a Thin-Walled Pressure Vessel

As a first order approximation of constants for Eqs. (2.1)–(2.3), we assumed a curvilinear coordinate system. We also neglected the role of the CJ and endocardium in supporting tensile stress. The CJ is a gel-like material that lacks tensile support. The CJ is reported to be a fraction of the stiffness of the myocardium, even under compression [12, 35, 36]. The endocardium is comprised of endothelial cells, estimated to have a stiffness of 1.5–5.6 kPa for isolated human aortic adult endothelial cells on a stiff substrate and could play a minor role in tensile support [37, 38]. Further simplifying our initial analysis, we assume the atrium to be a thin walled pressure vessel. With these assumptions, we use the Young–Laplace equation as a rough approximation of myocardial stress. Also, the myocardium is assumed incompressible, thereby requiring $\lambda_{rr}\lambda_{\theta\theta}\lambda_{zz} = 1$. We make a two-dimensional assumption since the radius of the atrium is much greater than the thickness of the myocardial layer. We assume load varies smoothly and that that there is no restriction by surrounding tissue along the contour of the myocardium modeled as a membrane. Also, since modeling the wall as a single layer of cells, we assumed that the stress is uniform across the myocardial thickness. We used the Young–Laplace equation for an equilibrium equation:

$$P = h(\kappa_\theta\sigma_{\theta\theta} + \kappa_z\sigma_{zz}), \tag{2.4}$$

where κ_θ is the radius of curvature in the circumferential direction for the semi-cylindrical atrial geometry, while κ_z is the radius of curvature along the axial direction, P is the inner applied pressure, with the assumption that the outer pressure is negligible, and h is the thickness, $\sigma_{\theta\theta}$ is the circumferential stress, and σ_{zz} is the axial stress in the myocardium. Note that due to incompressibility, we also assume:

$$r = \sqrt{r_o^2 - \frac{1}{\lambda_{zz}}(R_o^2 - R^2)}, \tag{2.5}$$

where the subscript, o, represents the outer radius.

2.2.6 Two-Dimensional Parameter Estimation

Equations (2.1)-(2.5). were used to relate the strain energy density function to the atrial diameter, curvature, length, and thickness for loaded and unloaded configurations. Material parameters were quantified using a nonlinear regression by minimizing the error function:

$$error = \sum_{i=1}^{N} \left(\frac{P_{measured}{}^{(i)} - P_{model}{}^{(i)}}{\bar{P}} \right)^2 \tag{2.6}$$

where $P_{measured}$ is the measured pressure, P_{model} is the predicted model pressure, i is a data point, and $\bar{P}$ is the average pressure for all of the data points. All calculations were performed in Matlab R2018b (The Mathworks, Inc., Natick, MA). Fits were performed using a nonlinear least-squares method to minimize errors between the models and the experiments.

2.2.7 2D Image and data Analysis for the 2D Approximation of Mechanical Properties Assuming a Thin-Walled Pressure Vessel

An image analysis was performed for each pressure step. Note that only the ventricle extends out-of-plane when viewing a cross-sectional area of the atrium in this study and was not evaluated in our study. To measure atrial area, we traced the atrium in ImageJ using the constriction at the AVC and AI as borders for the tracing [39]. To measure radius, the outer curvature (OC) and inner curvature (IC) of the atrium were separately traced and the coordinates were exported to Matlab. A midline of the atrium was established with a curvilinear coordinate system. The diameter of the atrium at half the centerline, Figure 2.1a. This measurement was then used for κ_θ and $\lambda_{\theta\theta}$. Curvature of the trace was used for κ_{zz}. We assume that a 0 pressure condition exists after application of the BDM and before cannulation. We consider the geometry under these conditions as an initial configuration, neglecting potential residual stress. Once cannulation occurs, there is typically a small increase in atrial area, which we assume is caused by a small increase in pressure as local tissue deforms at the cannulation site. We attempt to account for this by assuming the initial pressure value after cannulation is above 0, estimated based on extrapolating pressure from pressure-area curves. We would like to acknowledge that this can lead to some error when calculating constants in Eqs. (2.1)–(2.3). We do note that exclusion of the extrapolation changes the constants by less than 10%. Model Eqs. (2.1)–(2.3) were fit to data generated experimentally as explained above.

2.2.8 Three-Dimensional Imaging

We also perform a finite element analysis that requires three-dimensional geometry. Therefore, three dimensional imaging was performed on a representative 48 hpf Tg(myl7:eGFP) embryonic zebrafish heart (atrium and ventricle) with fluorescent myocardial cells using a laser-scanning confocal microscope (Zeiss LSM 800, Thornwood, NY). Z-stack spacing was set to 0.3 microns with a lateral resolution of 3.2 pixels/ micron. The resulting image consisted of discrete nuclei, representing individual cells in the myocardium, Figure 2.1d. Embryos were prepared and anesthetized in agarose + BDM solution as described above. Embryos were oriented ventral side down on a glass cover slip in such a way that the heart was as close to the objective lens as possible. A representative embryo was used for the three-dimensional image, as opposed to averaging multiple geometries since morphology is challenging to standardize at this stage in development. Note that we were unable to pressurize the heart on the confocal microscope due to technical challenges with cannulation on inverted microscopes. Therefore, the three-dimensional geometry was only used in the below finite element parameter estimation.

2.2.9 Finite Element Analysis

Since the two-dimensional analysis required many simplifying assumptions related to geometry, we also applied constants from the two-dimensional analysis to three-dimensional geometry reconstructed from the confocal z-stack of the atrium and ventricle for a representative embryo. Using the z-stack, the zebrafish heart was semi-automatically segmented using a lazy snapping algorithm created in a custom-written C++ code. Using VMTK software, the segmented two-dimensional-images were converted to a three-dimensional geometry, Figure 2.1e.The jagged surface of the reconstructed geometry was then smoothed using Meshmixer (Autodesk Inc.). FEA was performed to evaluate the experimental results using ABAQUS 6.14 (Simulia, RI, USA). The simulations were performed with 40,000 mesh elements, as determined after a mesh independence study. The zebrafish heart was modeled as a thin-layered geometry with a uniform thickness of 3 μm. The boundary conditions were set such that in all simulations, the ventricular outflow tract was fully constrained and the AI plane was set such that it was symmetric along the axial (normal) direction. The ventricular outflow boundary condition was far from points of measurement in the atrium.The AI boundary condition was chosen based on lack of movement of the AI along the axial direction seen during pressurization. Strain was probed at 10 points along the outer curvature of the atrium, indicated by the red arrows in Figure 2.1e. The maximum principal strain was converted to stretch ratios averaged across 10 points along the outer curvature to compare with experimental results. The maximum stretch ratio for experiments was determined by averaging the circumferential stretch ratios from each embryo for a pressure step. This was repeated for the axial stretch ratios. The greater value between axial and circumferential stretch ratio was considered the maximum stretch ratio and used for comparison against the FEA results.

2.3 Results

2.3.1 Mechanical Response of Atrium to Pressure Loading

For all embryos, the atrium visibly expands upon pressurization, Figure 2.2a and b. Cardiomyocytes along the OC and IC elongate and become thinner as the atrium increases in size. The cross-sectional area of the atrium increases steadily for pressures below 1 mmHg and normalized area values below 1.07, noting that physiological pressures at this stage in development are below 2 mmHg. Area changes are less as pressure increases above 2 mmHg, with an overall area increase of approximately 8% at 2 mmHg. For larger pressure values, area stretch trends are more variable, with a max increase of around 18% for a pressure of 7.5 mmHg, an over-pressurized state, Figure 2.2c.

2.3.2 Mechanical Properties and Parameter Estimation

Unknown parameters for Eqs. (2.1)-(2.3) were determined based on stretch ratios in curvilinear coordinates along the outer curvature of the atrium. Green strain increases proportionally in both axial and circumferential directions for a given pressure, indicating that the mechanical properties may be isotropic or transversely isotropic, Figure 2.3. The Neo-Hookean model, Eq. (2.1), is the

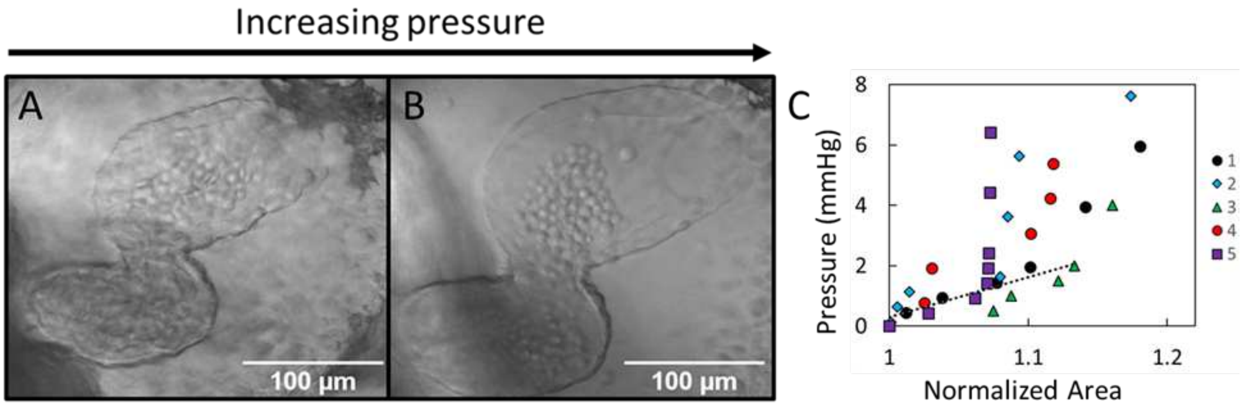

Figure 2.2: (a) Brightfield microscope image of the 48 hpf zebrafish heart before and after (b) pressurization to 10 mmHg. Note expansion of the atrium (larger upper chamber) as pressure increases. (c) Plot of pressure (mmHg) vs. normalized area (deformed area/unstressed area) for all 5 embryos combined. Normalized area increases as pressure increases, indicating expansion of the atrium under pressure. Trendline indicates linearity of points below 2 mmHg.

simplest model considered with a single parameter, C_H. Fitting this model results in an C_H of 32.23 ± 12.52 kPa (all best fit values are presented as ± standard deviation), Figure 2.4. The two-parameter reduced polynomial strain energy density function, Eq. (2.2), results in a C_S of 49.08 ± 19.28 kPa and C_{S1} of 11.47 ± 4.99, Figure 2.5. A two-parameter exponential model (C_I and C_{I1}) that assumes isotropy, Eq. (2.3), results in an average C_I is 17.54 ± 8.22 kPa, and C_{I1} is 21.72 ± 12.91, Figure 2.6. The large standard deviation demonstrates large variability between samples with this model. The Neo-Hookean model behavior deviates from experimental data at high strain; instead of an increasing slope, the Neo-Hookean model plateaus. The reduced polynomial and exponential functions from Eqs. (2.2) and (2.3) better depict the behavior seen for the atrial tissue. A summary of parameters is presented in Table 2.1.

2.3.3 Finite Element Analysis

We applied a Neo-Hookean and reduced polynomial model to the three-dimensional geometry of an embryonic zebrafish heart. The resulting simulated stretch ratios were compared to experiments to determine whether the above two-dimensional analysis can sufficiently capture three-dimensional behavior. Results are compared with experimental maximum stretch ratios averaged

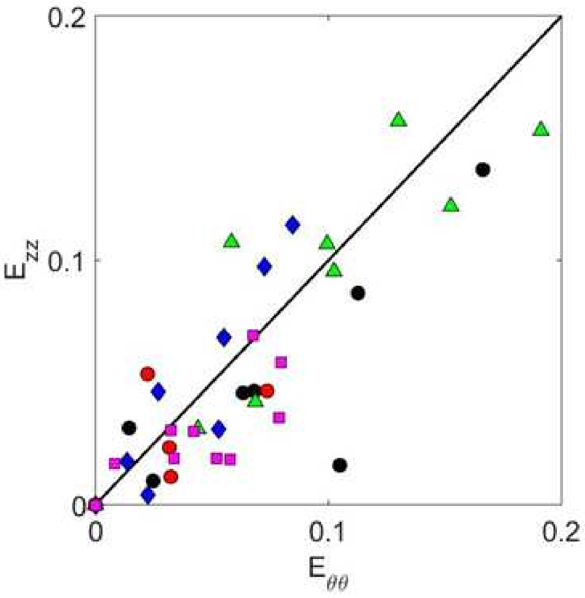

Figure 2.3: Plot of Green strain in the axial direction (E_{ZZ}) vs in the circumferential direction ($E_{\theta\theta}$) for all 5 embryos combined, a proportional increase of both indicates isotropy.

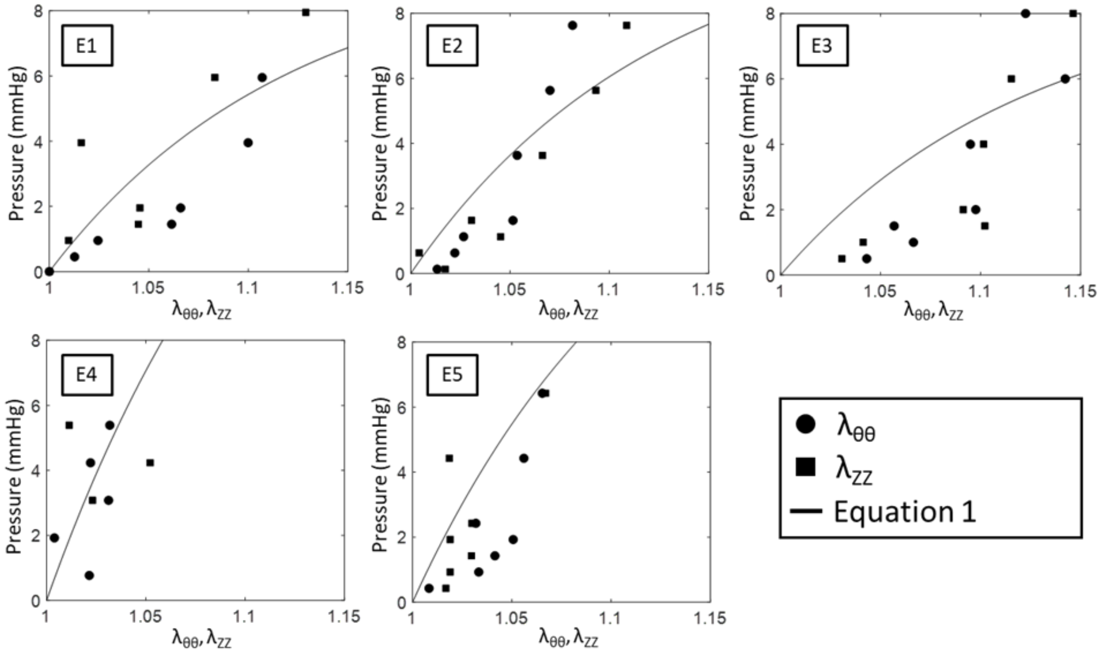

Figure 2.4: Plots of pressure (mmHg) vs. circumferential and longitudinal stretch (λ_{zz} and $\lambda_{\theta\theta}$) for each embryo. Line indicates Hookean model fit.

for five zebrafish along the OC, Figure 2.7. Neo-Hookean maximum stretch ratios coincide closely with experiments. In contrast, there is clear disparity between the reduced polynomial and exper-

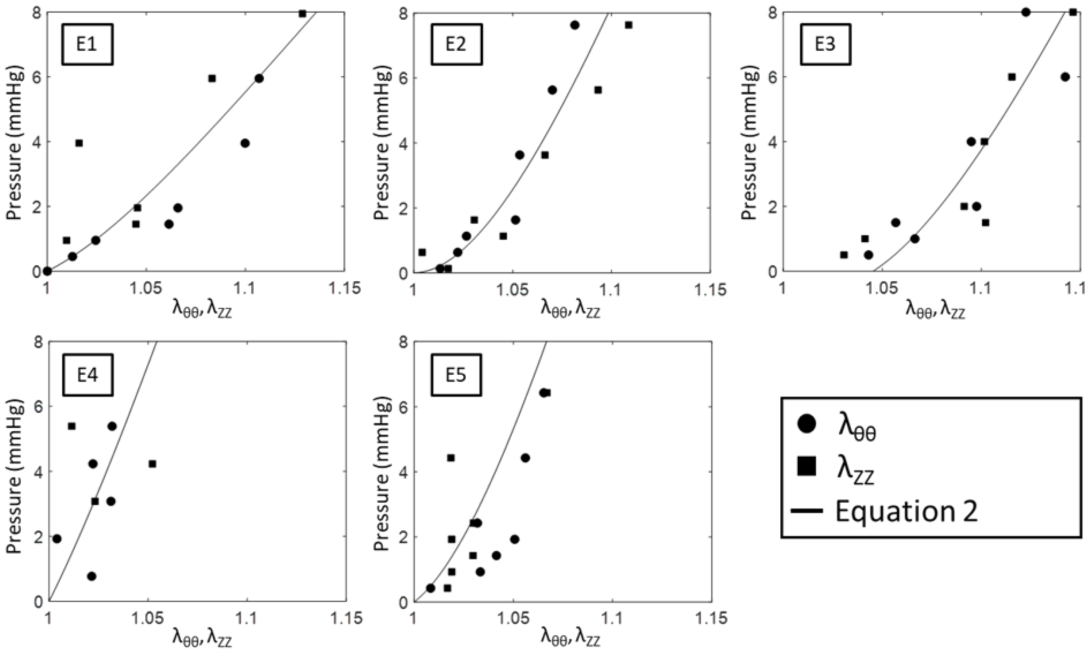

Figure 2.5: Plots of pressure (mmHg) vs. circumferential and longitudinal stretch (λ_{zz} and $\lambda_{\theta\theta}$) for each embryo. Line indicates Single Cell model fit.

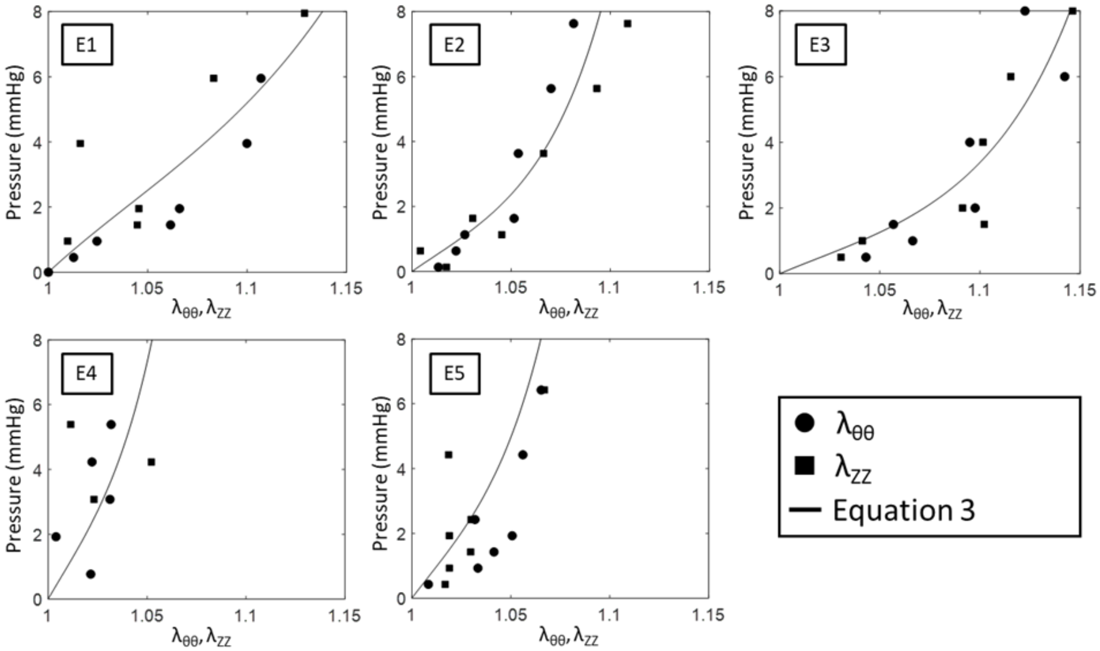

Figure 2.6: Plots of pressure (mmHg) vs. circumferential and longitudinal stretch (λ_{zz} and $\lambda_{\theta\theta}$) for each embryo. Line indicates Eq. (2.3) model fit.

Table 2.1: Coefficients generated from experimental model fits of Eq. (2.1) (Neo-Hookean), Eq. (2.2) (reduced polynomial), and Eq. (2.3) (exponential).

Equation	1	2		3	
Replicate	C_H (kPa)	C_S (kPa)	C_{S1}	C_I (kPa)	C_{I1}
1	14.71	15.49	3.17	10.43	5.81
2	32.64	60.00	14.98	15.62	22.39
3	30.39	49.90	15.10	11.04	12.69
4	49.96	60.00	10.57	30.47	38.17
5	33.46	60.00	13.52	23.15	29.56
Avg.	32.23	49.08	11.47	17.54	21.72
SD	12.52	19.28	4.99	8.22	12.91

imental strain results. The differences in maximum principal logarithmic strain between the two FEA models are reflected in contour maps, Figure 2.8. Neo-Hookean strain is greater along the OC, generally remaining in the 0.02 to 0.05 range for a pressure of 2 mmHg (Figure 2.8a). Reduced polynomial maximum principal strain ranges from 0 to 0.2 along the OC (Figure 2.8b). For both models, strain does increase above 0.05 near the AI, a potential artifact of the boundary condition. It also increases near the AVC along the IC of the atrium. Overall, the Neo-Hookean model strain approximately matched the experimental strain while the reduced polynomial model predicted strain much lower than what was seen in the two-dimensional experiments for physiological loads.

2.4 Discussion

We developed a technique to characterize the mechanical properties of the embryonic zebrafish heart, Figure 2.1. By inflating the atrium, we established a relationship between pressure and deformation, Figures 2.2 and 2.3. Through simplified assumptions, we show that the embryonic zebrafish atrium is best depicted by a nonlinear hyperelastic strain energy density function, Figures 2.4, 2.5, 2.6, and 2.7. Overall, we demonstrate an ability to quantify cardiac tissue deformation under tension for an applied inflation pressure in live embryonic zebrafish for the first time. The

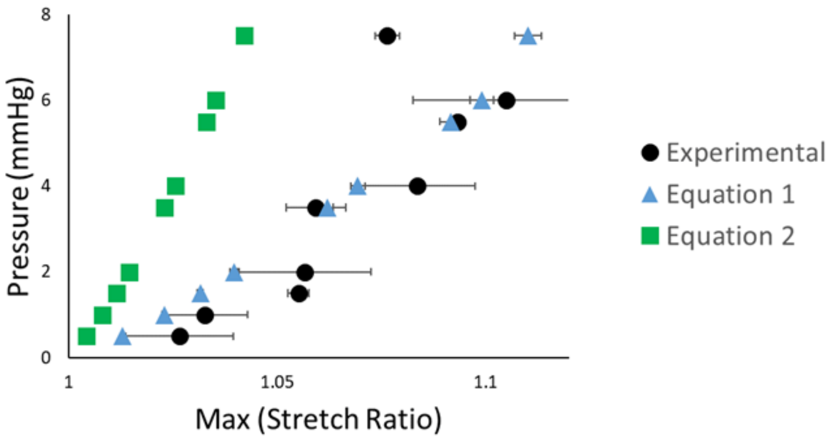

Figure 2.7: Plot of Pressure (mmHg) vs. maximum stretch ratios for experimental data, Reduced Polynomial simulation data, and Neo-Hookean simulation data. Error bars represent the standard error mean.

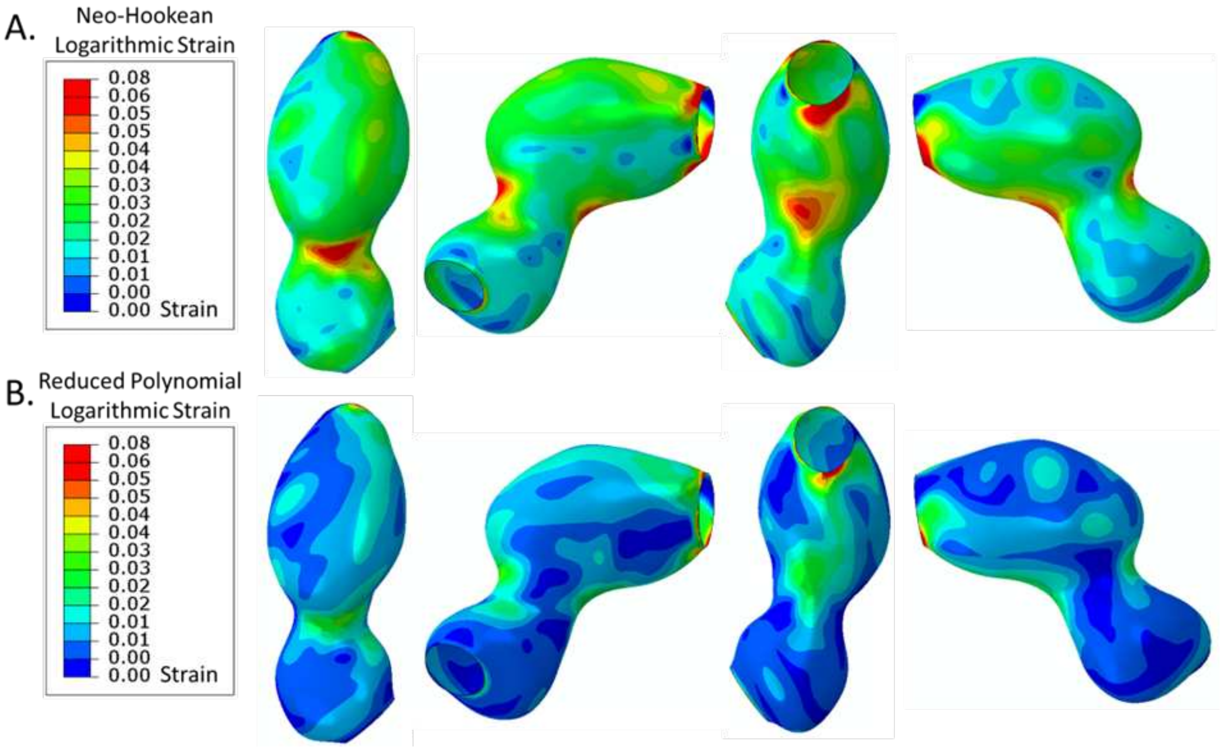

Figure 2.8: Three-dimensional max principal logarithmic strain map of a simulated 48 hpf zebrafish heart pressurized to 2 mmHg using a Neo-Hookean and Reduced Polynomial model. The top chamber in each individual strain map represents the atrium.

current approach enables the quantification of mechanical properties for high throughput zebrafish-specific genetic models, which could be applied to multiple stages of development.

Atrial stiffness in our study is higher, but on the same order of magnitude of values found for other species. At 48 hpf, we found a material constant of 32.23 ± 12.52 kPa for the zebrafish atrial wall based on a Neo-Hookean model, Eq. (2.1) (Table 2.1). Zebrafish at 48 hpf is equivalent to chicks at 45–52 hpf or Hamburger and Hamilton stages 12–14 [40, 41]. In the chick heart, myocardial stiffness has been shown to increase with embryonic age, estimated at 0.3 kPa/day between 2 and 6 days of development, as measured through aspiration [5]. Comparatively, others demonstrate a bimodal tissue modulus of either 1–6 kPa or 9– 14 kPa through AFM on explanted quail embryonic myocardium [42]. AFM experiments on isolated, non-contracting, neonatal rat cardiomyocytes produce modulus values of 6.5 ± 4.8 kPa [43]. Higher stiffness values found in our study, compared to other species, may be related to the surrounding intact tissue, which could constrain atrial deformation for the high loading conditions used in our study. We see lower stiffness for physiological pressure (< 2 mmHg). Overall, it appears that myocardial mechanical properties may be relatively conserved across species during early heart development.

Additional studies have quantified mechanical properties of embryonic intact heart tissue using other nonlinear isotropic models. Zamir et al. found mean values for C_I of 13.0 ± 5.6 Pa and C_{I1} values of 0.57 ± 0.34, when quantifying residual stress using Eq. (2.3) [35]. In comparison, we found values of 17.67 ± 7.05 kPa for C_I and 21.10 ± 13.94 for C_{I1} (Table 2.1). The large discrepancy in parameter values is likely due to the approach taken by Zamir et al. where they quantify residual stress under compressive conditions on a small scale. Here, mechanical properties are evaluated in an overstretched state under a tensile load for the overall tissue. Therefore, in the current work, subcellular filamentous actin and sarcomeres are pulled, similar to physiological, but elevated, loading conditions (although at a higher stress). Furthermore, Zamir et al. is using a different species in their analysis. Overall, the model from Zamir et al. depicted the behavior of the atrial tissue, despite the difference in species and the difference in material constants.

We postulate that mechanical properties of the intact zebrafish heart at 48 hpf is primarily driven by stretching of individual cardiomyocytes, especially since stiffness is similar to values found for single or collective cardiomyocytes. Sarcomeres have fully formed by 48 hpf in zebrafish and may provide tensile support [44]. In comparison, sarcomerogenesis takes longer in other species, including chick, where mechanical properties change (0.3 kPa/day) early in development [5]. Passive tension within sarcomeres is largely controlled by titin [45]. Connections with costameres, Z-discs, and intercalated discs would also contribute passive mechanical properties, particularly after sarcomerogenesis [46]. We speculate that some of these subcellular structures may be reaching a fully stretched state in our study, which may explain the stiffening of tissue during over-pressurization. Similar curves are seen as titin extends with stiffening occurring after a stretch ratio of 1.14 [45]. Speculation on the subcellular structures that support passive loads would need to be more rigorously tested in future studies.

We observed significant variation between replicates and between our two-dimensional and three-dimensional analysis. Reproducibility may be affected by the method used to quantify the 0 pressure condition, which can change material parameters by up to 10% (based on a comparison with and without extrapolation). Also, inconsistency in orientation of the zebrafish body affects cross-sectional planar measurements. Atrial area in the initial configuration varied by 13% in the present study. We expect additional errors in determining circumferential stretch ratios and curvature, since we do not account for out-of-plane morphology. Such errors may provide an explanation for discrepancies between the two- and three-dimensional analyses. Overall, three-dimensional, e.g. confocal, imaging during pressurization is expected to improve the variability and would likely lead to a more accurate estimation of material constants.

We note various limitations to our study. First, a continuum framework may not provide the best approach to model the embryonic heart due to the small size. In the current work, we neglect the contribution of the CJ, endocardium, and surrounding tissue in supporting tensile loads. This approximation may lead to higher predicted stiffness values compared to values that actually exist. A major assumption in the current work is that we can quantify mechanical properties based on a cross-sectional image of three-dimensional tissue using a simplified Young–Laplace equation. Although errors can arise, the current work still demonstrates a technique that could be combined with three-dimensional imaging for more accurate quantification, an approach that warrants future investigation. Mechanical properties may also be heterogeneous. Due to the size of the zebrafish embryonic heart, we did not control the boundary conditions. Lastly, there may also be residual stress in the tissue that we did not quantify due to the difficulty in handling the small-sized hearts of zebrafish. Studies using chick embryos demonstrate that residual stress is relatively small after looping, and therefore may not significantly impact the results [18]. Despite these limitations, we are able to still quantify mechanical properties of the embryonic zebrafish heart using a first order approximation, demonstrating an important technique that can be used to understand various potential phenotypes seen in zebrafish.

References

[1] Yunfei Shi, Jiang Yao, Gang Xu, and Larry A Taber. Bending of the looping heart: differential growth revisited. *Journal of biomechanical engineering*, 136(8), 2014.

[2] Norman Hu and E B Clark. Hemodynamics of the stage 12 to stage 29 chick embryo. *Circulation research*, 65(6):1665–1670, 1989.

[3] NORMAN Hu and BRADLEY B Keller. Relationship of simultaneous atrial and ventricular pressures in stage 16-27 chick embryos. *American Journal of Physiology-Heart and Circulatory Physiology*, 269(4):H1359—-H1362, 1995.

[4] Norman Hu, H Joseph Yost, and Edward B Clark. Cardiac morphology and blood pressure in the adult zebrafish. *The Anatomical Record: An Official Publication of the American Association of Anatomists*, 264(1):1–12, 2001.

[5] Stephanie Majkut, Timon Idema, Joe Swift, Christine Krieger, Andrea Liu, and Dennis E Discher. Heart-specific stiffening in early embryos parallels matrix and myosin expression to optimize beating. *Current Biology*, 23(23):2434–2439, 2013.

[6] Megan L McCain and Kevin Kit Parker. Mechanotransduction: the role of mechanical stress, myocyte shape, and cytoskeletal architecture on cardiac function. *Pflügers Archiv-European Journal of Physiology*, 462(1):89–104, 2011.

[7] David Sedmera, Tomas Pexieder, Vlasta Rychterova, Norman Hu, and Edward B Clark. Remodeling of chick embryonic ventricular myoarchitecture under experimentally changed loading conditions. *The Anatomical Record: An Official Publication of the American Association of Anatomists*, 254(2):238–252, 1999.

[8] Jay R Hove, Reinhard W Köster, Arian S Forouhar, Gabriel Acevedo-Bolton, Scott E Fraser, and Morteza Gharib. Intracardiac fluid forces are an essential epigenetic factor for embryonic cardiogenesis. *Nature*, 421(6919):172–177, 2003.

[9] Brennan Johnson, David Bark, Ilse Van Herck, Deborah Garrity, and Lakshmi Prasad Dasi. Altered mechanical state in the embryonic heart results in time-dependent decreases in cardiac function. *Biomechanics and modeling in mechanobiology*, 14(6):1379–1389, 2015.

[10] Timm Haack and Salim Abdelilah-Seyfried. The force within: endocardial development, mechanotransduction and signalling during cardiac morphogenesis. *Development*, 143(3):373–386, 2016.

[11] Jiang Yao, Victor D Varner, Lauren L Brilli, Jonathan M Young, Larry A Taber, and Renato Perucchio. Viscoelastic material properties of the myocardium and cardiac jelly in the looping chick heart. 2012.

[12] Evan A Zamir, Varahoor Srinivasan, Renato Perucchio, and Larry A Taber. Mechanical asymmetry in the embryonic chick heart during looping. *Annals of biomedical engineering*, 31(11):1327–1336, dec 2003.

[13] D E Ingber and I Tensegrity. Cell structure and hierarchical systems biology. *J. Cell Sci.*, 116, 2003.

[14] J A N Lammerding, Roger D Kamm, and Richard T Lee. Mechanotransduction in cardiac myocytes. *Annals of the New York Academy of Sciences*, 1015(1):53–70, 2004.

[15] Elizabeth A Schroder, Kimimasa Tobita, Joseph P Tinney, Jane K Foldes, and Bradley B Keller. Microtubule involvement in the adaptation to altered mechanical load in developing chick myocardium. *Circulation research*, 91(4):353–359, 2002.

[16] Rong-zhen Zhang, Anatoliy A Gashev, David C Zawieja, and Michael J Davis. Length-tension relationships of small arteries, veins, and lymphatics from the rat mesenteric microcirculation. *American Journal of Physiology-Heart and Circulatory Physiology*, 292(4):H1943–H1952, 2007.

[17] Tatyana G Kuznetsova, Maria N Starodubtseva, Nicolai I Yegorenkov, Sergey A Chizhik, and Renat I Zhdanov. Atomic force microscopy probing of cell elasticity. *Micron*, 38(8):824–833, 2007.

[18] E A Zamir and L A Taber. On the effects of residual stress in microindentation tests of soft tissue structures. *J. Biomech. Eng.*, 126, 2004.

[19] Jay D Humphrey. *Cardiovascular solid mechanics: cells, tissues, and organs*. Springer Science & Business Media, 2013.

[20] Kimimasa Tobita, Elizabeth A Schroder, Joseph P Tinney, Jason B Garrison, and Bradley B Keller. Regional passive ventricular stress-strain relations during development of altered loads in chick embryo. *American Journal of Physiology-Heart and Circulatory Physiology*, 282(6):H2386—-H2396, 2002.

[21] D L Bark, B Johnson, D Garrity, and L P Dasi. Valveless pumping mechanics of the embryonic heart during cardiac looping: Pressure and flow through micro-PIV. *Journal of Biomechanics*, 50:50–55, 2017.

[22] Glickman N. S., D. Yelon. Cardiac development in zebrafish: coordination of form and function. In: Seminars in Cell and Developmental Biology Elsevier, pp. 507–513, 2002.

[23] M. Westerfield. *The Zebrafish Book.* University of Oregon Press, Eugene, OR, 1995.

[24] Thomas Bartman, Emily C Walsh, Kuo-Kuang Wen, Melissa McKane, Jihui Ren, Jonathan Alexander, Peter A Rubenstein, Didier Y R Stainier, and Brigid Hogan. Early myocardial function affects endocardial cushion development in zebrafish. *PLoS biology*, 2(5):e129, 2004.

[25] CWTJ Herrmann, John Wray, F Travers, and T Barman. Effect of 2, 3-butanedione monoxime on myosin and myofibrillar ATPases. An example of an uncompetitive inhibitor. *Biochemistry*, 31(48):12227–12232, 1992.

[26] Socrates Dokos, Bruce H Smaill, Alistair A Young, and Ian J LeGrice. Shear properties of passive ventricular myocardium. *American Journal of Physiology-Heart and Circulatory Physiology*, 283(6):H2650—-H2659, 2002.

[27] D Y Stainier, Brant M Weinstein, H W 3rd Detrich, Leonard I Zon, and Mark C Fishman. Cloche, an early acting zebrafish gene, is required by both the endothelial and hematopoietic lineages. *Development*, 121(10):3141–3150, 1995.

[28] Brant M Weinstein, Derek L Stemple, Wolfgang Driever, and Mark C Fishman. Gridlock, a localized heritable vascular patterning defect in the zebrafish. *Nature medicine*, 1(11):1143–1147, 1995.

[29] C S H L Press. *Danieau's Solution (30×).* Cold Spring Harbor Protocols, New York, 2011.

[30] A G Holzapfel. *Nonlinear Solid Mechanics.* Wiley, New York, 2000.

[31] Philippe Tracqui and Jacques Ohayon. Transmission of mechanical stresses within the cytoskeleton of adherent cells: a theoretical analysis based on a multi-component cell model. *Acta Biotheoretica*, 52(4):323–341, 2004.

[32] Oon H Yeoh. Some forms of the strain energy function for rubber. *Rubber Chemistry and technology*, 66(5):754–771, 1993.

[33] A Delfino, N Stergiopulos, J E Moore Jr, and J-J Meister. Residual strain effects on the stress field in a thick wall finite element model of the human carotid bifurcation. *Journal of biomechanics*, 30(8):777–786, 1997.

[34] Hilmi Demiray and Raymond P Vito. A layered cylindrical shell model for an aorta. *International Journal of Engineering Science*, 29(1):47–54, 1991.

[35] E A Zamir and L A Taber. Material properties and residual stress in the stage 12 chick heart during cardiac looping. *J. Biomech. Eng.*, 126, 2004.

[36] Tzu-Wei Wang and Myron Spector. Development of hyaluronic acid-based scaffolds for brain tissue engineering. *Acta biomaterialia*, 5(7):2371–2384, 2009.

[37] K D Costa, A J Sim, and F C P Yin. Non-Hertzian approach to analyzing mechanical properties of endothelial cells probed by atomic force microscopy. *J. Biomech. Eng.*, 128, 2005.

[38] Paul A Janmey and Christopher A McCulloch. Cell mechanics: integrating cell responses to mechanical stimuli. *Annu. Rev. Biomed. Eng.*, 9:1–34, 2007.

[39] Caroline A Schneider, Wayne S Rasband, and Kevin W Eliceiri. NIH Image to ImageJ: 25 years of image analysis. *Nature methods*, 9(7):671–675, 2012.

[40] Viktor Hamburger and Howard L Hamilton. A series of normal stages in the development of the chick embryo. *Journal of morphology*, 88(1):49–92, 1951.

[41] Jörg Männer. Cardiac looping in the chick embryo: a morphological review with special reference to terminological and biomechanical aspects of the looping process. *The Anatomical Record*, 259(3):248–262, 2000.

[42] Adam J Engler, Christine Carag-Krieger, Colin P Johnson, Matthew Raab, Hsin-Yao Tang, David W Speicher, Joseph W Sanger, Jean M Sanger, and Dennis E Discher. Embryonic cardiomyocytes beat best on a matrix with heart-like elasticity: scar-like rigidity inhibits beating. *Journal of cell science*, 121(Pt 22):3794–3802, nov 2008.

[43] Evren U Azeloglu and Kevin D Costa. Cross-bridge cycling gives rise to spatiotemporal heterogeneity of dynamic subcellular mechanics in cardiac myocytes probed with atomic force microscopy. *American Journal of Physiology-Heart and Circulatory Physiology*, 298(3):H853—-H860, 2010.

[44] A M Ebert, G L Hume, K S Warren, N P Cook, C G Burns, M A Mohideen, G Siegal, D Yelon, M C Fishman, and D M Garrity. Calcium extrusion is critical for cardiac morphogenesis and rhythm in embryonic zebrafish hearts. *Proceedings of the National Academy of Sciences of the United States of America*, 102(49):17705 LP – 17710, dec 2005.

[45] I Makarenko, C A Opitz, M C Leake, C Neagoe, M Kulke, J K Gwathmey, F Del Monte, R J Hajjar, and W A Linke. Passive stiffness changes caused by upregulation of compliant titin isoforms in human dilated cardiomyopathy hearts. *Circulation research*, 95(7):708–716, 2004.

[46] Allen M Samarel. Costameres, focal adhesions, and cardiomyocyte mechanotransduction. *American Journal of Physiology-Heart and Circulatory Physiology*, 289(6):H2291—-H2301, 2005.

Chapter 3

Aim 2: 3D Patterns of Strain Depend on Specific Hemodynamic Cues

3.1 Introduction

Early heart development is a complex process involving an interplay of stresses generated from blood flow. Through mechanotransduction, these stresses are transmitted through the tissue to act as mechanical cues which generate cellular responses that inform normal development. The transmission of stress is dependent on the material properties of the heart tissue, which is comprised of individual cells and the surrounding extracellular matrix (ECM). The components of the ECM, cell-ECM junctions, cytoskeletal components, and cell-cell junctions all contribute to the transmission and modulation of stress. As such, mechanotransduction is sensitive to perturbation, which may lead to drastic deformations.

Animal studies have shown that modified hemodynamic stress alters development through this process [1–6]. Hove et. al. have shown that blocked blood flow at the heart inlet or outlet via placement of a small bead lead to drastic developmental defects such as failure to loop, unformed bulbus, and collapsed inflow and outflow tracts [7]. Another group performed outflow tract banding, to increase hemodynamic load, and vein ligation, to decrease hemodynamic load, in embryonic chick hearts [8–10]. This resulted in changes in heart wall mechanical properties and defects such as left heart hypoplasia, double outlet right ventricle, and persistent truncus arteriosus. In addition, early heart development is particularly sensitive to mechanical stress, as malformations that manifest earlier have potential to compound to more severe defects later in development [5, 11].

An alternative to manipulating hemodynamics through physical means, is to directly manipulate the blood itself. Blocking transcription of the erythropoiesis modulating gene, *gata1*, through injection of an antisense morpholino oligonucleotide (MO), prevents the formation of red blood cells, thus decreasing blood hematocrit to zero and blood viscosity by 90% [6, 12]. Reduction of blood viscosity via *gata1* MO has been shown to alter hemodynamics, specifically the oscillatory flow across the atrioventricular canal [13]. However, resistance decreases with viscosity according to Poiseuille's Law, as such, the pressure that the heart must pump against decreases as well [14].

Here, we leverage the *gata1* MO to deplete red blood cells in embryonic zebrafish and employ a previously developed pressurization technique to investigate the effect of decreased blood pressure, resulting from decreased viscosity, on the mechanical response of the zebrafish embryonic heart tissue.

3.2 Methods

3.2.1 Zebrafish Embryo Preparation

Adult zebrafish were maintained according to Westerfield [15]. Ethical approval was provided by the Institutional Animal Care and Use Committee at Washington University in St. Louis. Embryos were collected from adults generated from crosses of *Tg(myl7:eGFP)*, green fluorescent myocardium; and *Tg(kdrl:mCherry)*, red fluorescent endocardium. Embryos were grown up in egg water prepared from Instant Ocean Sea Salts (Blacksburg, VA) (egg water) [15]. Embryos were dechorionated prior to experiments and transferred to a 1X Tyrode's solution (142 mM NaCl, 4.7 mM KCl, 10 mM HEPES, 10 mM Glucose, 1 mM $MgCl_2$, 1.8 mM $CaCl_2$) containing 25 mM Warfarin and 30 mM BDM. For experiments at 72 hpf, naturally dechorionated embryos were transferred to a solution of egg water containing 25 mM Warfarin and 40 mM BDM. Embryos were incubated in Tyrode's/Warfarin/BDM solution until the hearts ceased contracting and an additional 20 mins to allow for complete relaxation of the myocardium.

3.2.2 *Gata1* Knockdown by Morpholino

Gata1 MO (sequence 5'-CTGCAAGTGTAGTATTGAAGATGTC-3') was prepared by Gene-Tools. Approximately one nanoliter of 1 mM *gata1* MO dissolved in nuclease free water was injected at the one to four cell embryonic stage. Red blood cell depletion at 2 dpf was used as an indicator of morpholino success.

3.2.3 Cannula preparation

Borosilicate glass capillaries (World Precision Instruments, inc., Sarasota, FL, TW150F-4) were pulled using a micropipette puller (Sutter Instrument Company, Novato, CA, P-30), with the following settings: heat=880, pull=400, trip micrometer=2. Capillary tips were then sharpened on a micropipette beveler with a fine abrasive plate (Sutter Instrument Company, Novato, CA, BV-10). Sharpening was necessary because the embryo skin stretches significantly if poked by a dull cannula. Additionally, beveling increases the tip inner diameter because the tip is sharpened at a 25-30° angle (Figure 3.1), which alleviates clogging.

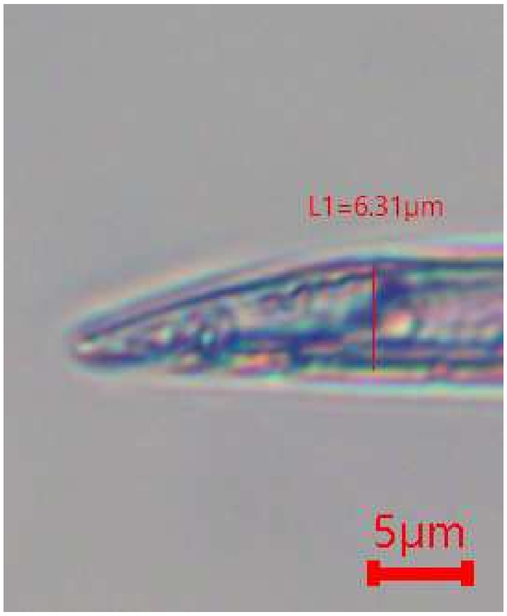

Figure 3.1: Beveled cannula tip.

Cannula dimensions at the tip are critical to achieving a successful pressurization. Inner tip diameters that are less than 5μm will have low flow ($\leq 1\mu$L/min), as such they will generate pressure in the heart very slowly. Tip diameters that are too large ($\geq 10\mu$m), although they will cause quick pressure changes, will be difficult to push through embryonic tissue. Beveling the tip helps to achieve both easier tissue puncture and higher flow rate.

Upon cannulation, the glass tip will stick to any tissue it contacts; this will cause difficulty in puncturing the skin and the cannula will inevitably become clogged. To alleviate this, cannulae were treated with a non-specific binding blocking agent by incubating in 1% casein for at least 30 minutes.

Cannulae were filled with an injection solution of 1X Tyrode's, 25 mM Warfarin Salts (Sigma Aldrich, St. Louis, MO, A4571), and 0.2% 0.52μm $\varnothing$ red fluorescent microspheres (Thermo Scientific, Fremont, CA, Fluoro-Max R500) to visualize flow. This was best achieved by submerging the cannula tip in injection solution and allowing capillary flow to slowly fill the needle tip. Backfilling the cannula by inserting a long needle from the end opposite the tip and applying syringe pressure often resulted in clogging, whereas capillary filling automatically filters as the solution is slowly pulled into the tip. After the injection solution has travelled past the neck of the glass cannula, the remaining empty volume was filled with additional injection solution. After filling, cannulae were stored with their tips submerged in 1% casein solution or in incubation solution prior to cannulation.

3.2.4 Embryo orientation and mounting

Embryos are embedded in 200μL of a 1% low-melt agarose solution of 1X Tyrode's (pH 7.2) containing 30 mM BDM. Zebrafish embryos were positioned for optimal imaging and so that the cannulae can approach from a fixed direction and angle. Prior to the agarose setting, embryos are held in the correct orientation as close to the gel surface as possible. This limits the gel that the cannula must travel through to reach the embryo, which helps to prevent clogging and tracking of the cannula in unintended directions. To prevent floating of agarose drop, the glass slide used for mounting was scored. A silicone isolator was bonded to the surface of the glass slide to contain the agarose. Embryo temperature was held at $28.5°$C by a temperature controlled stage insert (Bioscience Tools, Highland, CA). To keep the agarose from drying out, and for eventual immersion of the objective, 100μL of incubation solution was applied to the top of the agarose droplet after hardening.

3.2.5 Cannulation

Cannulae were fitted onto an acrylic needle holder (World Precision Instruments, inc., Sarasota, FL, MPH315) which was connected to a reservoir and pressure controller (Fluigent, Ile-de-France, France, 25 mbar Flow-EZ) via a silicone tube. A 5 mL syringe was placed inline between the needle and reservoir to facilitate pre-filling of the system and removal of bubbles. To achieve accurate readings from the pressure controller, it is critical that all leaks are sealed and compliance sources (air bubbles) are removed.

A 40X water immersion objective with a 3.3 mm long working distance (Olympus, Waltham, MA, LUMPLFLN40XW) was lowered onto the agarose embedded embryo until a column of incubation solution was formed between the objective and agarose gel. After focusing on the sinus venosus region, the cannula tip was directed into the water column via a motorized micromanipulator (Zaber, Vancouver, BC) and lowered into the imaging plane.

Prior to cannulation, the pressure control system was calibrated by roughly levelling the reservoir fluid surface with the cannula tip/mounted embryo and zeroing the Flow-EZ pressure controller through its local menu. Red fluorescent microspheres were used to visualize flow in the cannula under an upright microscope (Olympus, Waltham, MA, FV1000). The reservoir level was manually adjusted until the microspheres stopped moving, at which point the pressure at the tip was assumed to be zero.

To successfully approach and puncture the embryo skin, the cannula angle was set as shallow as possible, approximately 30°. The goal was to approach the embryo surface such that the cannula was tangent to the yolk at the puncture point. If the cannula approach angle is too high, it is likely to lethally puncture the yolk. The target puncture area for embryos of all ages, was an approximately 50 μm^2 region at the confluence of the cardinal veins or just posterior to the sinus venosus. This area was positioned so the cannula would press against and stretch the skin while moving tangentially to and just over the surface of the yolk until it punctured the vessel. If the cannula was sufficiently sharp, the skin did not stretch too much before puncture. Immediately after puncture, the cannula was drawn back so the tip was not pressing against the vessel wall. If the yolk was punctured or significant red blood cell leakage was observed, the embryo was discarded.

3.2.6 Pressurization and Imaging

Upon successful cannulation, pressure was cycled from zero to 0.25 mmHg, and repeated five times with one minute between each cycle. After cycling, pressure was set back to 0 mmHg. After two minutes of resting to return to pressure equilibrium, pressure was again increased to 0.25 mmHg. Another two minute rest period was completed before the heart was imaged. Pressurization continued as shown in Table 3.1, until the heart ruptured, abruptly changed shape, or the maximum pressure in the sequence was reached. Image stacks were obtained at each pressure step using an FV1000 confocal microscope (Olympus, Waltham, MA). Z-stack spacing was set to 2 microns with a lateral resolution of 2.5 pixels/micron.

3.2.7 Image processing and Deformation Analysis

For each z-stack, the zebrafish heart was semi-automatically segmented using a lazy snapping algorithm created in a custom-written C++ code. The segmented two-dimensional-images were converted to a three-dimensional geometry from which heart volume and surface areal changes were extracted. A matlab motion tracking algorithm was used to extract the deformation gradient F between the 3D geometries generated for each pressure step $F = \frac{\partial x}{\partial X}$. A line connecting the apex of the ventricle with the center of the ventricular outlet was used to define a reference from which all deformations in the ventricle were generated. This was repeated for the atrium. The extracted deformations were converted into Green-Lagrange strains ((3.1)) using the 3D image obtained at the zero pressure step, which was collected after pressure cycling but before increasing pressure to a positive value.

Table 3.1: Pressurization sequence.

Pressure step	Applied Pressure (mmHg)
No manipulation	-
Post-cannulation	0.00
Post-cycling	0.00
1	0.25
2	0.50
3	0.75
4	1.00
5	1.25
6	1.50
7	1.75
8	2.00
9	2.50
10	3.00
11	4.00
12	5.00
13	6.00
14	8.00
15	10.0

$$E = \frac{1}{2}(F^T \cdot F - I) \tag{3.1}$$

3.2.8 Regional Strain and Cell Density Analysis

To visualize heart expansion and strain patterns, max eigen values for 2-dpf, 3-dpf, and *gata1* MO treated 3-dpf hearts were projected onto the 3D geometry of each heart (n=2 for all groups). Max eigen values were extracted from six regions within the point cloud comprising the heart geometry, the atrial outer curvature, atrial inner curvature, inferior atrioventricular junction (AVJ), superior atrioventricular junction, ventricular inner curvature, and ventricular outer curvature (Figure 3.2). Hearts were visualized in 3D using Imaris software (BitPlane, South Windsor, CT, USA) where cell number and mean cell-to-cell three nearest-neighbor (cell-to-cell distance) values were extracted from each region.

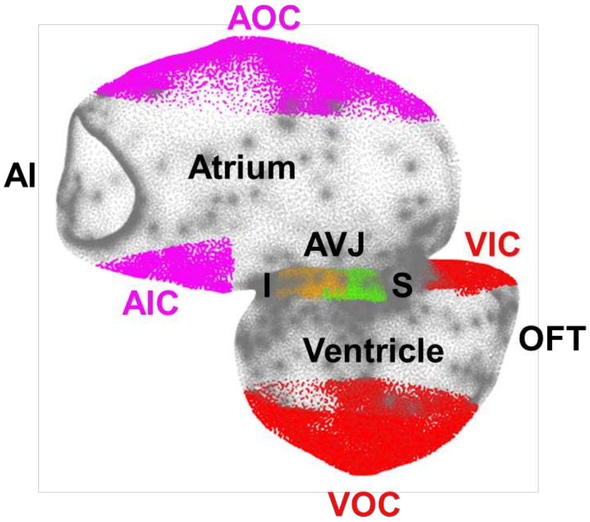

Figure 3.2: Data were extracted from points comprising the 3D geometry of the 2-dpf heart in six regions, atrial outer curvature (AOC), atrial inner curvature (AIC), inferior atrioventricular junction (AVJ I), superior atrioventricular junction (AVJ S), ventricular inner curvature (VIC), and ventricular outer curvature (VOC). Blood flows from the atrial inlet (AI) to the out flow tract (OFT).

3.3 Results

3.3.1 Ventricular and Atrial Expansion Upon Pressure Loading

Areal stretch ratio increased upon pressurization for all replicates and ranged from 3% to 34% depending on location. Max ventricle areal stretch ratio for 2 dpf embryos was 1.06 for both embryos, with a pressure change of 1.25 and 2 mmHg for each embryo (Figure 3.3a). Max areal stretch was lower for 3-dpf ventricles at 1.04 for both and pressure changes of 2 and 3 mmHg (Figure 3.4a). *Gata1* MO treated embryos demonstrated the highest stretch of all ventricles at 1.07 for both embryos for pressure changes of 1 and 1.75 mmHg (Figure 3.5a).

Max areal stretch ratio was more variable for embryo atria. For 2-dpf embryos, areal stretch was 1.06 and 1.04, with pressure changes of 1.25 and 2 mmHg, respectively (Figure 3.3b). At 3-dpf, areal stretch for each atrium was 1.03 and 1.34, with pressure changes of 3 and 2 mmHg, respectively (Figure 3.4b). *Gata1* MO treated embryos had max areal stretch ratios of 1.14 and 1.16, with pressure changes of 1 and 1.75 mmHg, respectively (Figure 3.5b).

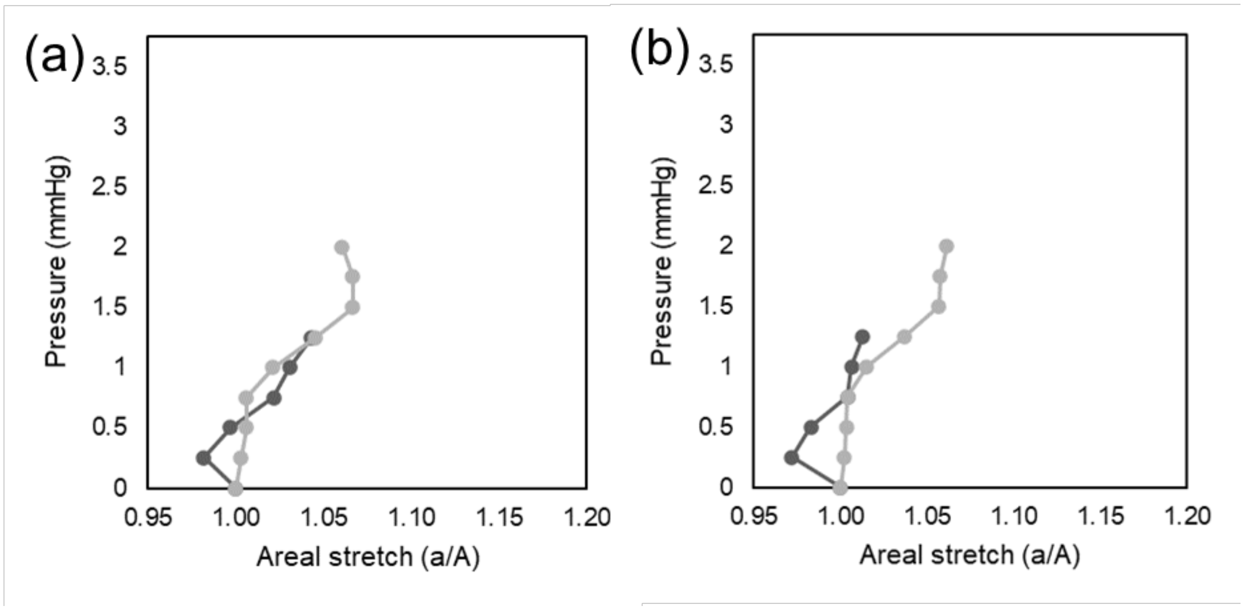

Figure 3.3: (a) 2-dpf ventricle pressure (mmHg) vs. stretch (a/A) (n=2). (b) 2-dpf atria pressure (mmHg) vs. stretch (a/A) (n=2). Areal stretch is calculated as the deformed state, a, divided by the initial non-deformed state, A.

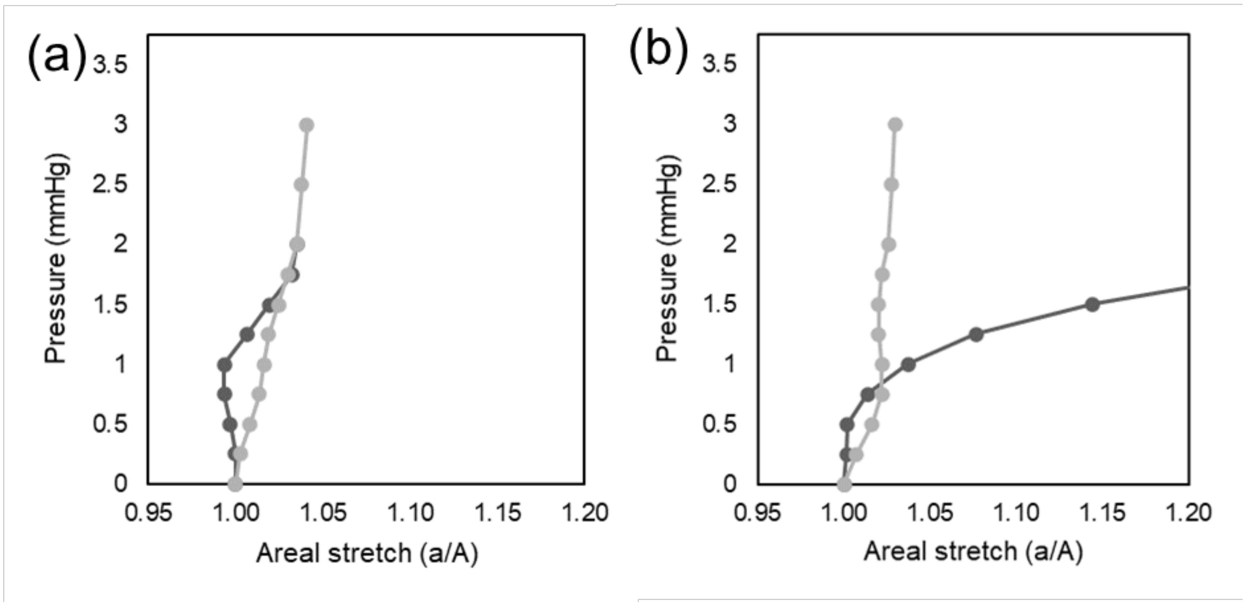

Figure 3.4: (a) 3-dpf ventricle pressure (mmHg) vs. stretch (a/A) (n=2). (b) 3-dpf atria pressure (mmHg) vs. stretch (a/A) (n=2). Areal stretch is calculated as the deformed state, a, divided by the initial non-deformed state, A.

Overall, 3-dpf hearts expanded across a greater pressure range before failure than 2-dpf and *gata1* MO treated 3-dpf embryos. *Gata1* MO treated atria had the most areal stretch per unit pressure, excepting the atrium of 3-dpf embryo 2. *Gata1* MO treated ventricle areal stretch resembled

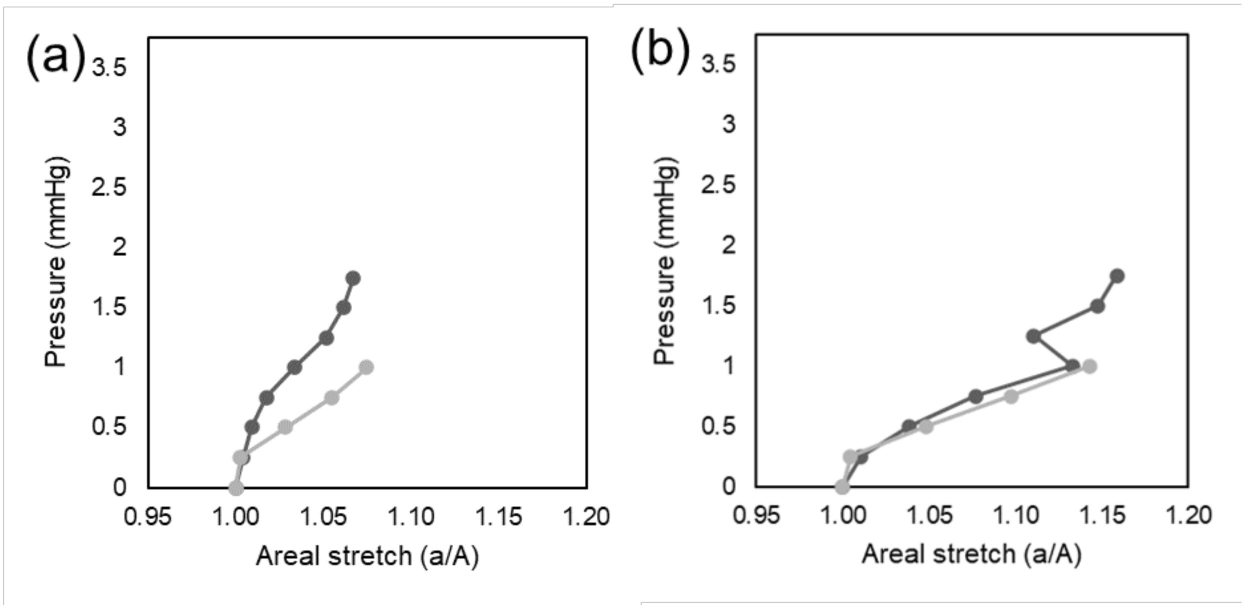

Figure 3.5: (a)*Gata1* MO treated 3-dpf ventricle pressure (mmHg) vs. stretch (a/A) (n=2). (b)*Gata1* MO treated 3-dpf atria pressure (mmHg) vs. stretch (a/A) (n=2). Areal stretch is calculated as the deformed state, a, divided by the initial non-deformed state, A.

that of 2-dpf ventricles, with a lower slope than 3-dpf ventricles, which stretched the least of all chambers.

3.3.2 Strain Mapping and Regional Analysis

The greatest differences in max eigen value (max positive strain) between 2 and 3-dpf hearts were observed along the atrial outer curvature, where 2-dpf max strain reached 0.2, which is twice that observed in 3-dpf, Figure 3.6a. These high strain values in 2-dpf outer curvatures are reflected in the strain maps, Figure 3.7 and Figure 3.8 as compared to 3-dpf outer curvatures in Figure 3.9 and Figure 3.10.

Additionally, max strain in the superior AVJ region was 0.3 for 2-dpf and 0.1 for 3-dpf (Figure 3.11c). Strain trended higher for 3-dpf in the atrial inner curvature and ventricular outer curvature (Figure 3.6c). Cell-to-cell distance did not have an observed change between 2 and 3-dpf hearts. However, values were higher for both ages in the atrial outer curvature as compared to other regions (Figure 3.6a).

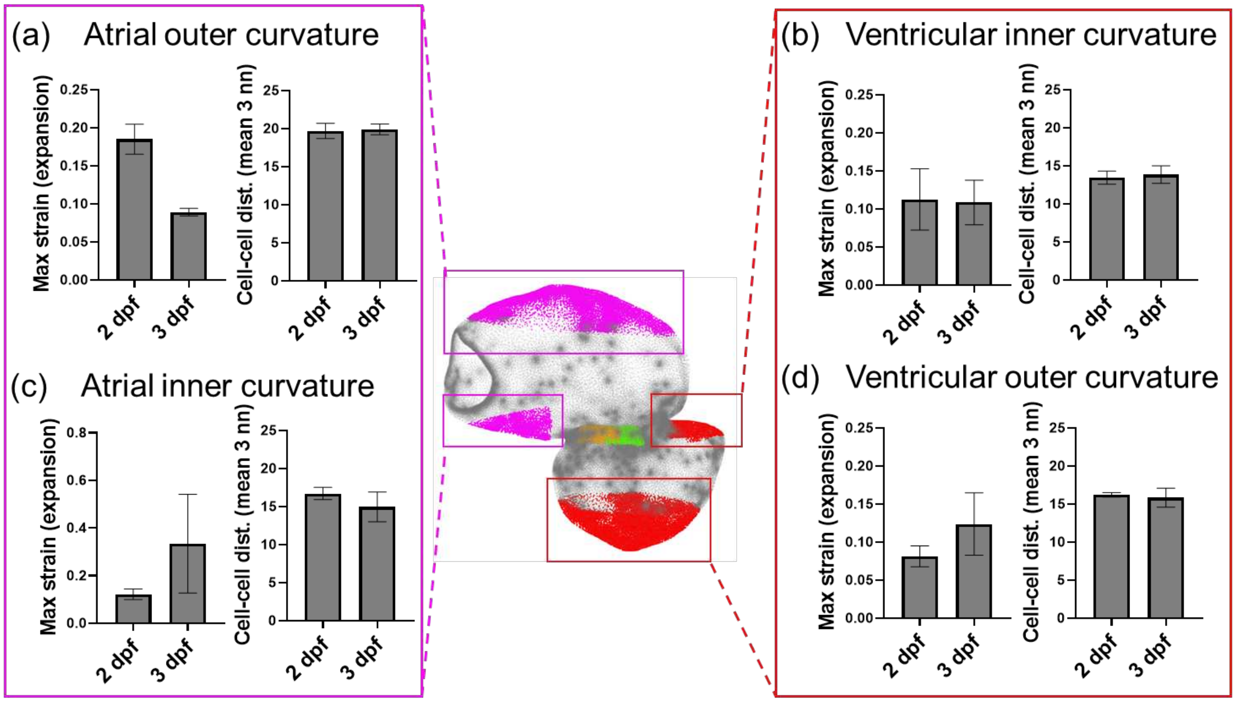

Figure 3.6: Regional max strains (eigen values) and cell-to-cell distances for 2 and 3-dpf hearts.

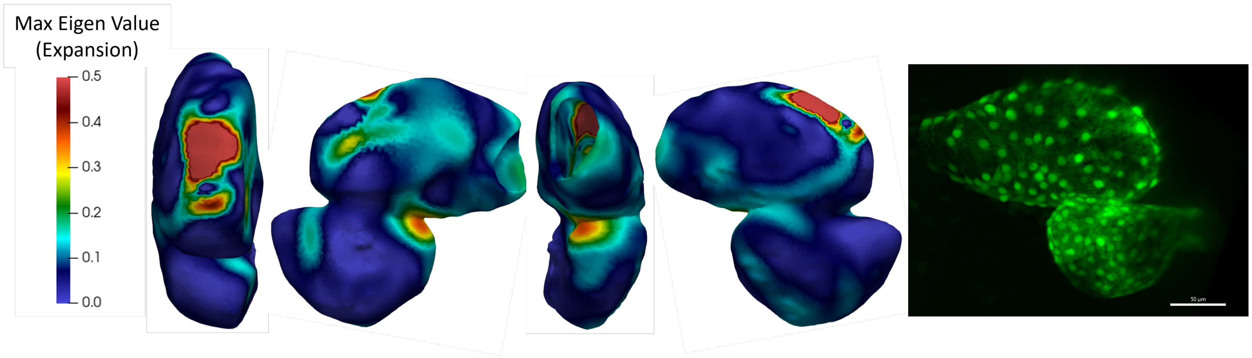

Figure 3.7: 2-dpf (embryo 1) max strain (eigen value) map for a pressurized embryonic zebrafish heart. Projection angle (from left to right): top (atrium), right side, front (atrial inlet), left side, left side 3D image.

In all regions, *gata1* MO treated 3-dpf hearts displayed higher max strains than in untreated 3-dpf hearts (Figure 3.12), specifically in the atrial outer curvature where max strain for *gata1* MO treated 3-dpf was 0.17 to 0.42 and untreated 3-dpf was 0.09 to 0.08 (Figure 3.12a). High strain along the atrial outer curvature is observable in max strain maps for both *gata1* MO treated embryos (Figure 3.13, Figure 3.14). In the superior AVJ region, *gata1* MO treated embryos displayed notably higher strain than untreated (0.14 to 0.47 compared to 0.06 to 0.11, Figure 3.15c).

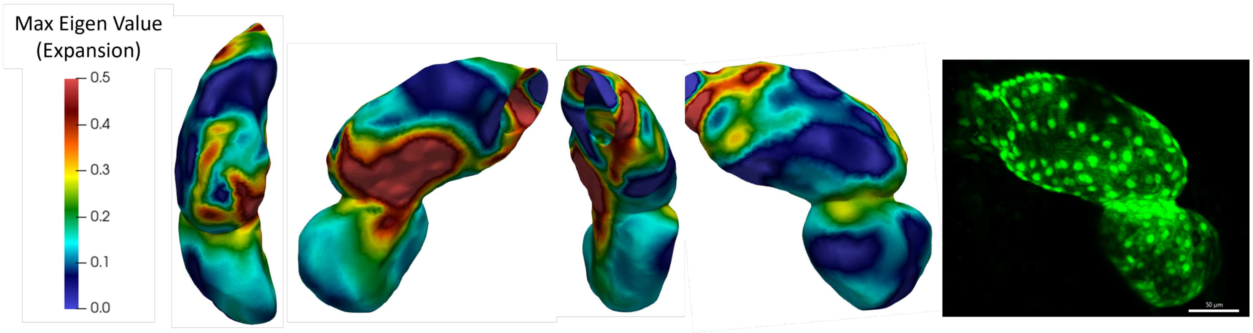

Figure 3.8: 2-dpf (embryo 2) max strain (eigen value) map for a pressurized embryonic zebrafish heart. Projection angle (from left to right): top (atrium), right side, front (atrial inlet), left side, left side 3D image.

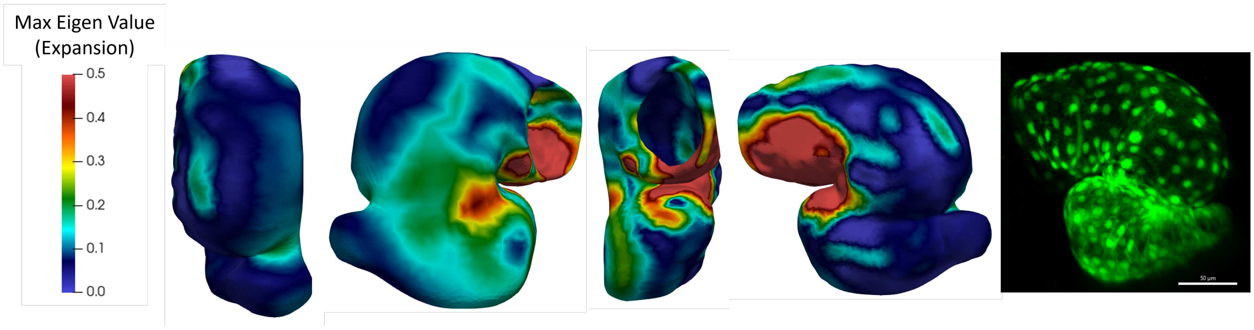

Figure 3.9: 3-dpf (embryo 1) max strain (eigen value) map for a pressurized embryonic zebrafish heart. Projection angle (from left to right): top (atrium), right side, front (atrial inlet), left side, left side 3D image.

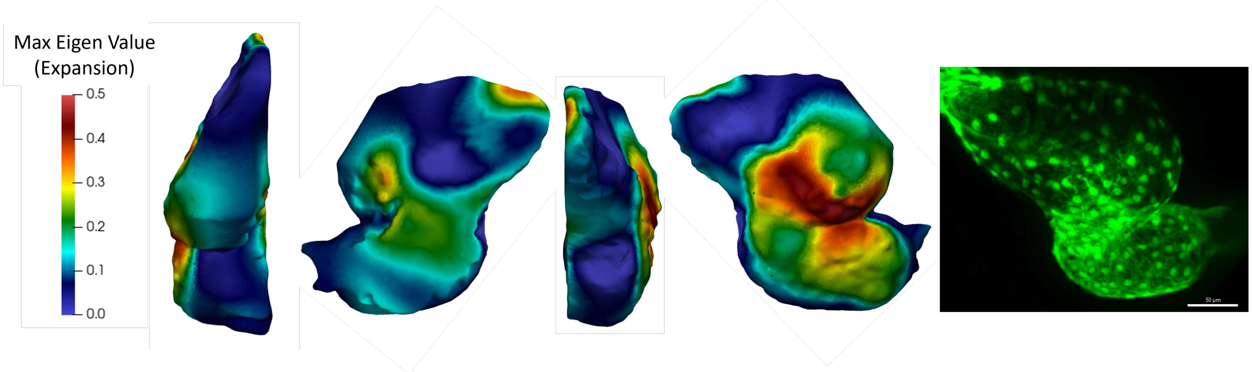

Figure 3.10: 3-dpf (embryo 2) max strain (eigen value) map for a pressurized embryonic zebrafish heart. Projection angle (from left to right): top (atrium), right side, front (atrial inlet), left side, left side 3D image.

Differences in cell-to-cell distance were discernible in the atrial outer curvature, where *gata1* MO treated embryos ranged from 21.2 to 23.2 microns between cells and untreated from 19.2 to 20.6 microns between cells, the ventricular inner curvature (12.4 to 12.5 microns for *gata1* MO

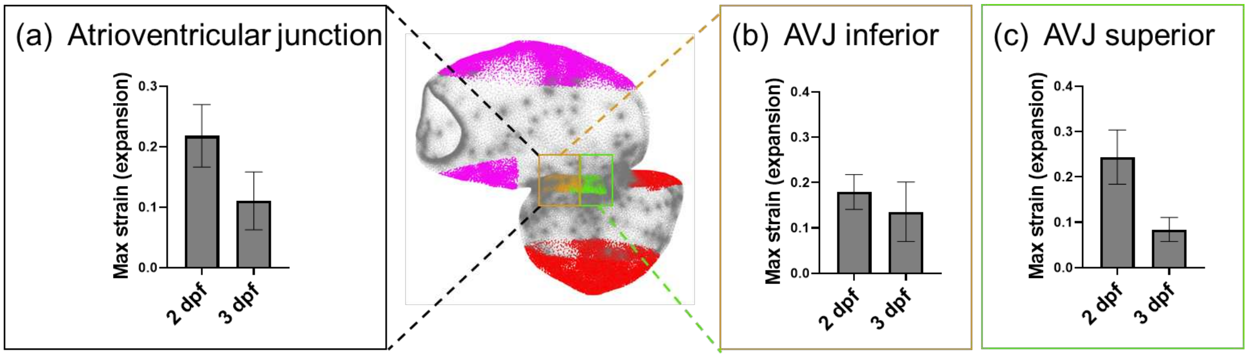

Figure 3.11: Atrioventricular junction max strain (eigen value) for 2 and 3-dpf embryonic zebrafish hearts (a) in the inferior (b) and superior (c) regions.

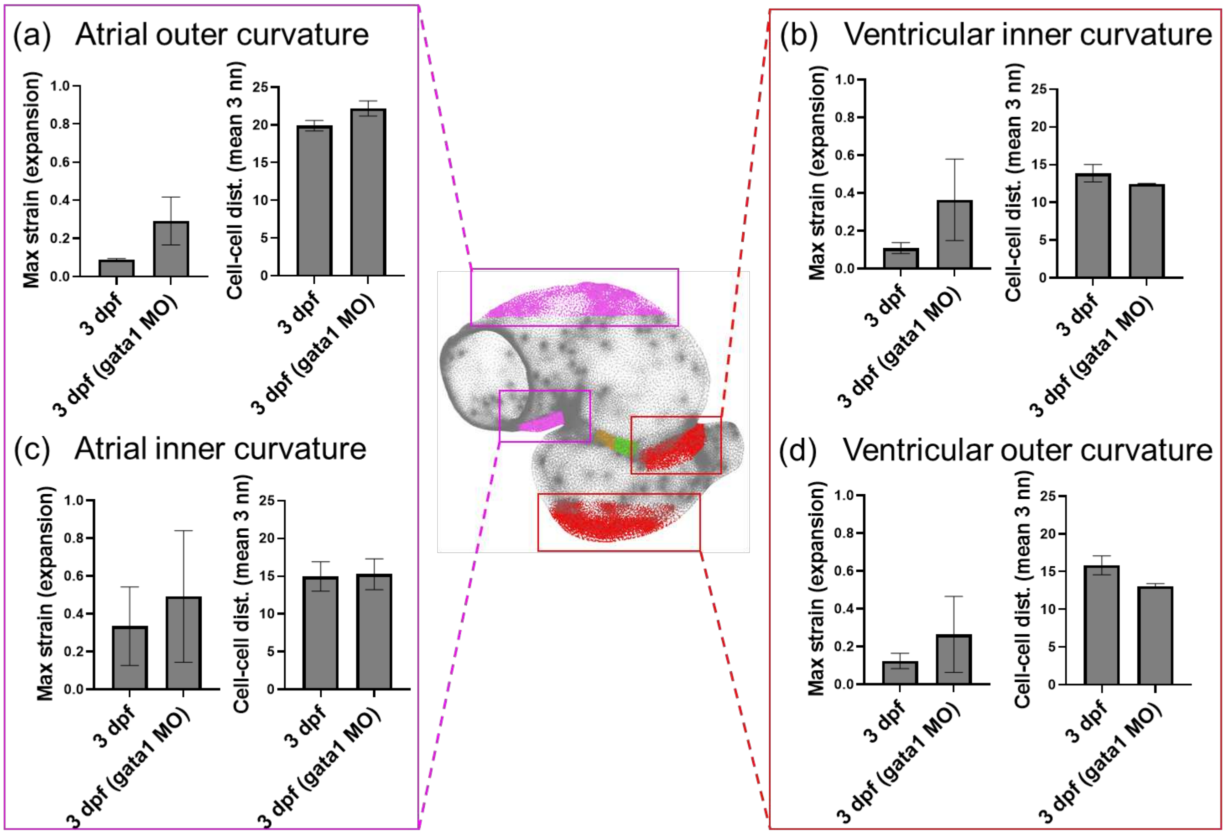

Figure 3.12: Atrioventricular junction max strain (eigen value) for 3-dpf and 3-dpf, *gata1* MO treated embryonic zebrafish hearts (a) in the inferior (b) and superior (c) regions.

treated, 12.7 to 15 microns for untreated), and the ventricular outer curvature (12.8 to 13.4 microns for *gata1* MO treated, 14.6 to 17.1 microns for untreated) (Figure 3.15 a, b, and d).

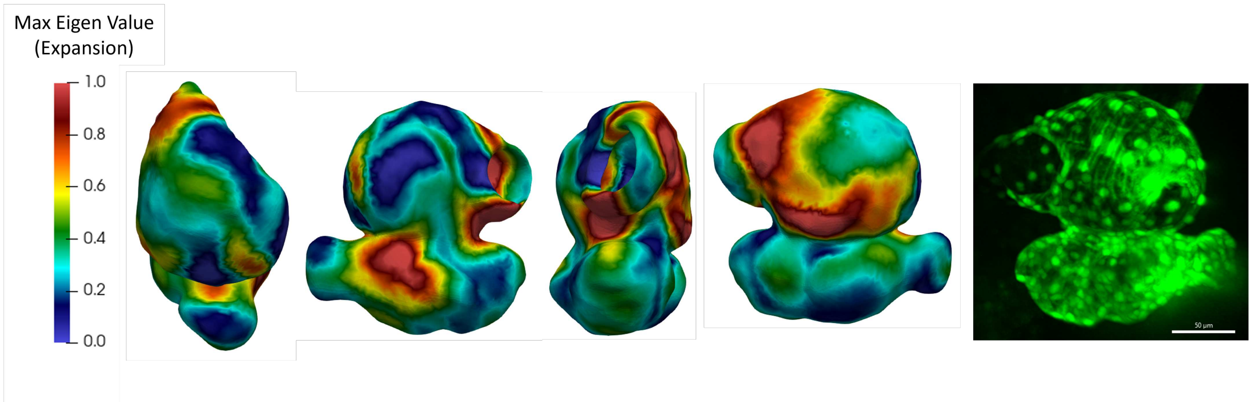

Figure 3.13: *Gata1* MO treated 3-dpf (embryo 1) max strain (eigen value) map for a pressurized embryonic zebrafish heart. Projection angle (from left to right): top (atrium), right side, front (atrial inlet), left side, left side 3D image.

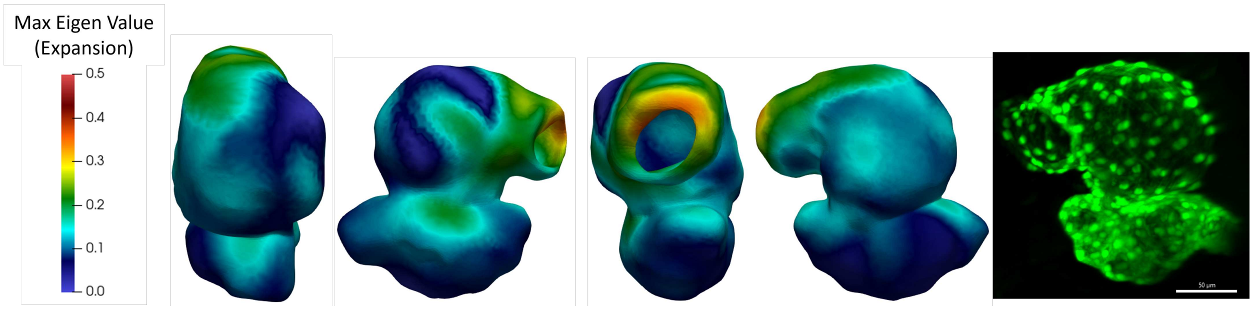

Figure 3.14: *Gata1* MO treated 3-dpf (embryo 2) max strain (eigen value) map for a pressurized embryonic zebrafish heart. Projection angle (from left to right): top (atrium), right side, front (atrial inlet), left side, left side 3D image.

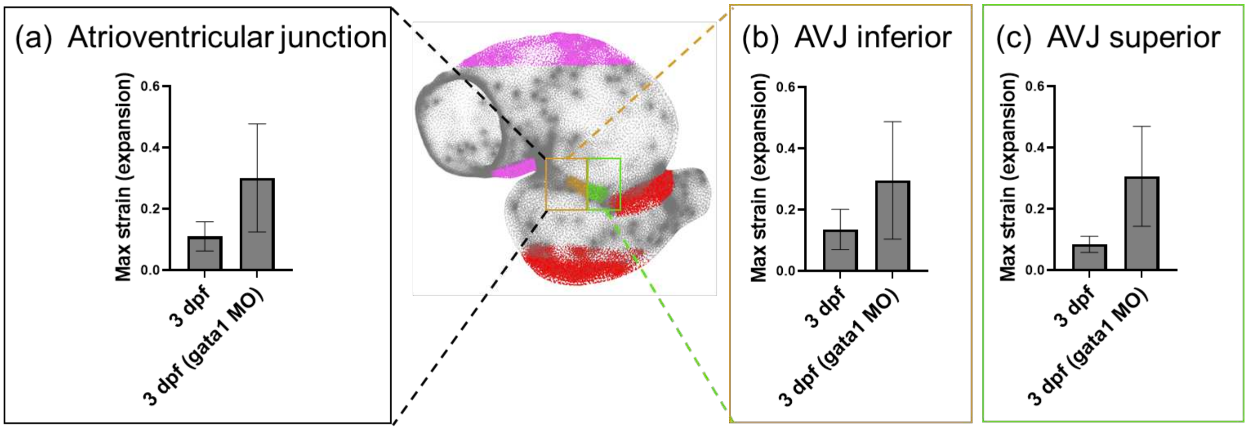

Figure 3.15: Atrioventricular junction max strain (eigen value) for 3-dpf and 3-dpf, *gata1* MO treated embryonic zebrafish hearts (a) in the inferior (b) and superior (c) regions.

3.4 Discussion

We established that controlled pressurization of the embryonic zebrafish vasculature is a viable technique for generating deformation in the embryonic heart. In this work, three-dimensional imaging during pressurization provides strain information for the entire heart and in all directions. Furthermore, *gata1* MO knockdown of red blood cell formation provides information on how altered hemodynamics causes increased strain in the heart tissue, relative to controls.

Although we do not directly measure stiffness, by comparing strain during pressurization throughout development and between specific regions, we can locate areas of relatively increased or decreased stiffness. We note that overall, the atrium deforms more than the ventricle. This may be in part due to geometry. The atrium is larger than the ventricle, therefore the atrial wall will undergo less stress than the myocardium under the same pressure according to LaPlace's law, $P = h\kappa\sigma$, where P is pressure, h is thickness, κ is the radius of curvature, and σ is stress.

We measured decreased strain in the AVJ region from 2 to 3 dpf. During this time, the endocardial cushions are forming in the valve region, which may decrease deformability. At 2 dpf, cardiac jelly accumulates in the AVJ region and by 3 dpf, endocardial migration has occurred leading to increased cell numbers at the AVJ [16]. Cell-to-cell mean three nearest neighbor distance, a measure of cell density, stayed constant from 2 to 3 dpf. This indicates that cell proliferation (hyperplasia) or growth (hypertrophy) is not significantly altering strain with age.

Gata1 MO treated embryos developed under low arterial pressure, based on Poiseuille's Law assumptions. In these embryos, we observed increased strain compared to 3 dpf controls. In the context of developing cardiomycytes, this finding is significant. Cardiomyocytes are highly sensitive to mechanical stress and are largely responsible for morphological rearrangements during embryonic heart development. Neonatal rat cardiomyocytes biaxially strained by 13% had altered gene expression which resulted in reduction of action potential duration [17, 18]. Strain has also been shown to alter physical and electrical coupling of cardiomyocytes through altered expression of gap-junction genes [19–22]. We show strain increases for *Gata1* MO treated over control embryos as high as 79% in the atrial outer curvature and 77% in the AVJ region. Given this large increase in strain, we speculate that stiffness changes have occurred.

References

[1] Jingchun Yang and Xiaolei Xu. α-Actinin2 is required for the lateral alignment of Z discs and ventricular chamber enlargement during zebrafish cardiogenesis. *The FASEB Journal*, 26(10):4230–4242, 2012.

[2] Dorothee Bornhorst, Peng Xia, Hiroyuki Nakajima, Chaitanya Dingare, Wiebke Herzog, Virginie Lecaudey, Naoki Mochizuki, Carl-Philipp Heisenberg, Deborah Yelon, and Salim Abdelilah-Seyfried. Biomechanical signaling within the developing zebrafish heart attunes endocardial growth to myocardial chamber dimensions. *Nature Communications*, 10(1):4113, 2019.

[3] Courtney Peshkovsky, Ronald Totong, and Deborah Yelon. Dependence of cardiac trabeculation on neuregulin signaling and blood flow in zebrafish. *Developmental Dynamics*, 240(2):446–456, 2011.

[4] Leigh Ann Samsa, Chris Givens, Eleni Tzima, Didier Y R Stainier, Li Qian, and Jiandong Liu. Cardiac contraction activates endocardial Notch signaling to modulate chamber maturation in zebrafish. *Development*, 142(23):4080–4091, 2015.

[5] Brennan Johnson, David Bark, Ilse Van Herck, Deborah Garrity, and Lakshmi Prasad Dasi. Altered mechanical state in the embryonic heart results in time-dependent decreases in cardiac function. *Biomechanics and modeling in mechanobiology*, 14(6):1379–1389, 2015.

[6] Julien Vermot, Arian S Forouhar, Michael Liebling, David Wu, Diane Plummer, Morteza Gharib, and Scott E Fraser. Reversing blood flows act through klf2a to ensure normal valvulogenesis in the developing heart. *PLoS biology*, 7(11):e1000246, 2009.

[7] Jay R Hove, Reinhard W Köster, Arian S Forouhar, Gabriel Acevedo-Bolton, Scott E Fraser, and Morteza Gharib. Intracardiac fluid forces are an essential epigenetic factor for embryonic cardiogenesis. *Nature*, 421(6919):172–177, 2003.

[8] Madeline Midgett, Sevan Goenezen, and Sandra Rugonyi. Blood flow dynamics reflect degree of outflow tract banding in Hamburger-Hamilton stage 18 chicken embryos. *Journal of the Royal Society, Interface*, 11(100):20140643, nov 2014.

[9] Sandra Rugonyi, Carley Shaut, Aiping Liu, Kent Thornburg, and Ruikang K Wang. Changes in wall motion and blood flow in the outflow tract of chick embryonic hearts observed with optical coherence tomography after outflow tract banding and vitelline-vein ligation. *Physics in medicine and biology*, 53(18):5077–5091, sep 2008.

[10] Madeline Midgett and Sandra Rugonyi. Congenital heart malformations induced by hemodynamic altering surgical interventions. *Frontiers in physiology*, 5:287, aug 2014.

[11] Richard P Harvey. Cardiac looping—an uneasy deal with laterality. In *Seminars in cell and developmental biology*, volume 9, pages 101–108. Elsevier, 1998.

[12] Jenna L Galloway, Rebecca A Wingert, Christine Thisse, Bernard Thisse, and Leonard I Zon. Loss of Gata1 but Not Gata2 Converts Erythropoiesis to Myelopoiesis in Zebrafish Embryos. *Developmental Cell*, 8(1):109–116, 2005.

[13] Emilie Heckel, Francesco Boselli, Stéphane Roth, Alice Krudewig, Heinz-Georg Belting, Gilles Charvin, and Julien Vermot. Oscillatory flow modulates mechanosensitive klf2a expression through trpv4 and trpp2 during heart valve development. *Current biology*, 25(10):1354–1361, 2015.

[14] Elie Nader, Sarah Skinner, Marc Romana, Romain Fort, Nathalie Lemonne, Nicolas Guillot, Alexandra Gauthier, Sophie Antoine-Jonville, Céline Renoux, Marie-Dominique Hardy-Dessources, et al. Blood rheology: key parameters, impact on blood flow, role in sickle cell disease and effects of exercise. *Frontiers in physiology*, 10:1329, 2019.

[15] M. Westerfield. *The Zebrafish Book*. University of Oregon Press, Eugene, OR, 1995.

[16] DYR Stainier, D Beis, B Jungblut, and T Bartman. Endocardial cushion formation in zebrafish. In *Cold Spring Harbor symposia on quantitative biology*, volume 67, pages 49–56. Cold Spring Harbor Laboratory Press, 2002.

[17] Erol Saygili, Obaida R Rana, Esra Saygili, Hannes Reuter, Konrad Frank, Robert HG Schwinger, Jochen Muller-Ehmsen, and Carsten Zobel. Losartan prevents stretch-induced electrical remodeling in cultured atrial neonatal myocytes. *American Journal of Physiology-Heart and Circulatory Physiology*, 292(6):H2898–H2905, 2007.

[18] Obaida R Rana, Carsten Zobel, Esra Saygili, Klara Brixius, Felix Gramley, Thomas Schimpf, Karl Mischke, Dirk Frechen, Christian Knackstedt, Robert HG Schwinger, et al. A simple device to apply equibiaxial strain to cells cultured on flexible membranes. *American Journal of Physiology-Heart and Circulatory Physiology*, 294(1):H532–H540, 2008.

[19] Tzong-Luen Wang, Yung-Zu Tseng, and Hang Chang. Regulation of connexin 43 gene expression by cyclical mechanical stretch in neonatal rat cardiomyocytes. *Biochemical and biophysical research communications*, 267(2):551–557, 2000.

[20] Kiyomi Yamada, Karen G Green, Allen M Samarel, and Jeffrey E Saffitz. Distinct pathways regulate expression of cardiac electrical and mechanical junction proteins in response to stretch. *Circulation research*, 97(4):346–353, 2005.

[21] Kou-Gi Shyu, Chia-Chi Chen, Bao-Wei Wang, and Peiliang Kuan. Angiotensin ii receptor antagonist blocks the expression of connexin43 induced by cyclical mechanical stretch in cultured neonatal rat cardiac myocytes. *Journal of molecular and cellular cardiology*, 33(4):691–698, 2001.

[22] Amit J Shanker, Kiyomi Yamada, Karen G Green, Kathryn A Yamada, and Jeffrey E Saffitz. Matrix protein–specific regulation of cx43 expression in cardiac myocytes subjected to mechanical load. *Circulation research*, 96(5):558–566, 2005.

Chapter 4

Aim 3: Early Heart Pumping Behavior

4.1 Introduction

The method used by the early heart to pump blood is limited by its tubular structure that operates without the assistance of valves or sequentially contracting chambers. It is made up of 3 distinct layers: an inner blood-contacting cellular monolayer of endocardial cells, a middle viscous gel-like layer called the cardiac jelly, and an outer contractile monolayer of cardiomyocytes. This early heart tube pumps in a peristaltic-like manner, in that sequential contraction of the myocardial cells results in a blood volume-displacing wave [1, 2]. However, high impact studies suggest alternative behavior, known as impedance pumping, characterized by elastic waves that travel through the tube wall while interacting with each other and the fluid contained within the tube [3, 4]. When the waves align constructively, they can produce forward flow. Experiments that best support this concept involve increasing body temperatures, which increase heart rate and thus cardiac output. In these experiments, red blood cell velocity exceeds the velocity of the contractile wave, implying flow is not only dictated by volume displacement. Additionally, red blood cell velocity does not increase linearly with heart rate, implying there may be contractile frequencies at which impedance mismatch occurs, resulting in increased or decreased flow rate. Importantly, the mechanical properties of the heart wall have the potential to influence this pumping, since these properties dictate wave speed and since wave reflections require a stiff inlet and outlet to the heart [5]. There is lack of agreement in the field as to what pumping method drives early blood flow, despite the importance in dictating hemodynamic stress [3, 5–7]. However, most support the perspective that pumping is the result of a combination of peristaltic, impedance, and potentially unknown pumping modes [5, 6].

Here, we propose several experiments to examine the pumping method of the early heart tube. Using a fine-tipped cannula and pressure controller, we attempt to induce impedance pumping through pressure pulsing. Furthermore, we closely analyze tube heart pumping mechanics under increased stress and we determine an as of yet unknown response by the tube heart where the endocardial closure is adjusted in response.

4.2 Methods

4.2.1 Zebrafish Preparation and Imaging

Wild-type zebrafish were bred according to Westerfield [8]. Embryos were collected from adult breeding pairs and allowed to develop to 24 hours post-fertilization while in 28.5°C egg water (Instant Ocean Sea Salts, Blacksburg, VA). Embryos were mounted on a glass slide in 1% low-melt agarose to arrest movement. A temperature controlled stage insert (Bioscience Tools, Highland, CA) was used to precisely control temperature from 24 to 34°C. After the desired temperature was reached, a 10 minute equalisation period was passed to allow heart rate to stabilize. Images were obtained at each degree for a total of 10 image sets using an Olympus BX61WI upright microscope and 40X water immersion objective with a resolution of 2.54 pixels/micron. A high-speed camera (Mega Speed, Manitoba, Canada) was used to capture approximately five heart beats at 1500 frames per second. Zebrafish embryos were positioned in the frame such that the tube heart was parallel to the imaging plane and to track red blood cell flow for the length of the heart.

4.2.2 Red Blood cell and Closure Tracking

A max intensity projection image set for five cycles was generated by subtracting the ensemble median in ImageJ, Fiji, thus making the red blood cells easier to track as white circles against a black background (Figure 4.1). Automated red blood cell tracking was performed in ImageJ using TrackMate [9, 10]. Tracks were manually edited to remove tracks generated from wall movement or non-RBC particles. In some cases, cells were manually tracked if automated tracking was unsuccessful. Red blood cell velocities were averaged over across five cycles to generate an ensemble average of one cycle length. Inlet, middle, and outlet regions were selected by separating the heart into three equal regions of interest using a custom Matlab code. RBC tracking was only performed for two embryos.

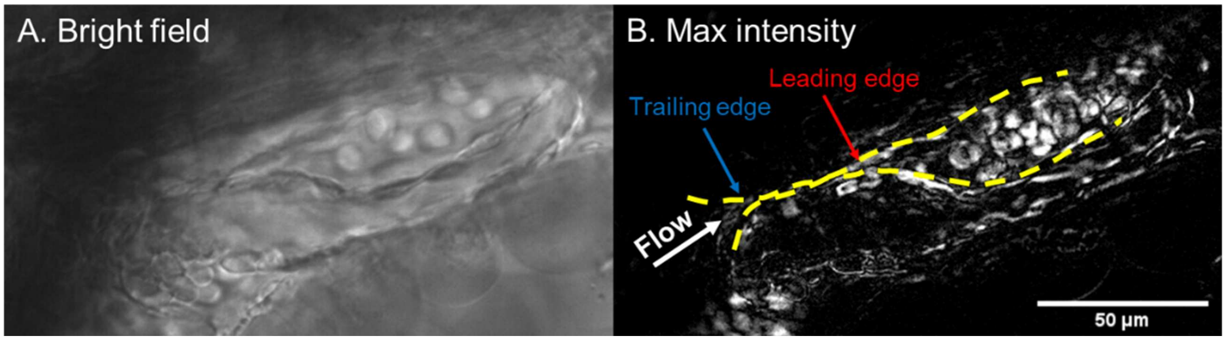

Figure 4.1: (a) Unprocessed Bright field image of 24 hour post-fertilization zebrafish heart.(b) Background subtracted image. Dashed yellow lines indicate endothelial wall boundary. White/gray circles are red blood cells. Leading-edge (red arrow) is at the front of the closure length. Trailing-edge (blue arrow) is at the rear of the closure length.

Closure length was measured in ImageJ by manually tracing the closure from the trailing-edge to the leading-edge for five cycles and averaging for each temperature. This was repeated at the inlet, middle, and outlet or end cycle. The inlet closure length was defined at the moment in the cycle when the trailing-edge first appears, the middle as the moment when the entire closure length is visible halfway through the closure transit time, the outlet or end cycle closure length was defined as the moment the leading-edge reached the end of the heart or closure travel length. Closure tracking was performed for six embryos. The leading and trailing-edges were tracked by selecting the front or rear of the endothelial closure at ten points as it traveled the length of the heart tube.

4.2.3 Impedance Pulsing

A glass cannula with tip outer diameter of 5 microns was inserted at the atrial inlet of a 24 hpf zebrafish heart using a motorized micromanipulator (Figure 4.2). Pulses at a rate of 2 Hz were applied separately at amplitudes (pressure) of 0.1, 0.5, and 1.0 mmHg with a 25 mbar pressure controller (Flow-EZ, Fluigent, France) (Figure 4.3). Pulse length as % of cycle was applied at

5, 10, 20, 30, and 40%. This was performed on a single zebrafish for five minutes at the lowest amplitude (0.1 mmHg) and 40% pulse length, then stepping down in pulse length until the lowest pulse of 5%, and repeating for 0.5 and 1 mmHg. The highest pressure (1 mmHg) was purposefully tested last.

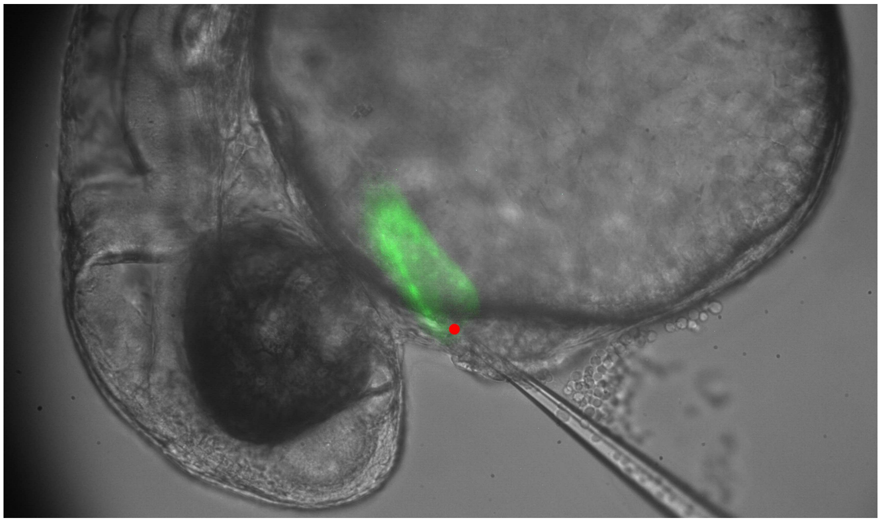

Figure 4.2: 24 hour post-fertilization zebrafish image. Zebrafish head is on bottom-left, dark circles indicate eyes. Green fluorescence represents tube heart myocardium. Red dot indicates tip of cannula where pressure pulse originates. Glass cannula is visible to bottom right of red dot.

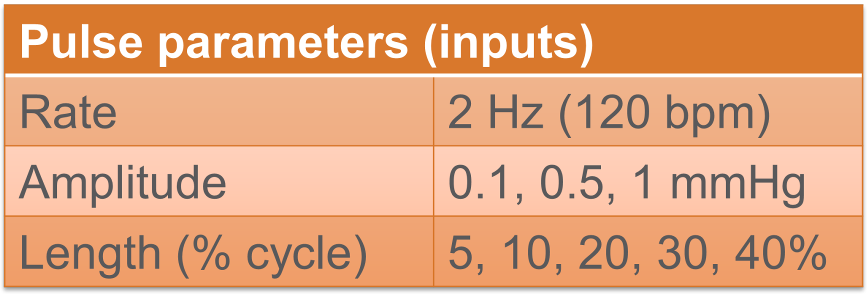

Pulse parameters (inputs)	
Rate	2 Hz (120 bpm)
Amplitude	0.1, 0.5, 1 mmHg
Length (% cycle)	5, 10, 20, 30, 40%

Figure 4.3: Applied pressure pulse parameters. Rate was kept constant at 2 Hz. Amplitude (pressure) and pulse length (% cycle) length were varied.

4.3 Results

Attempts to induce impedance pumping through pressure pulsing did not produce any forward blood flow. Only slight movement in the myocardium was detected at the greatest pulse amplitude of 1 mmHg. However, the pulse rate detected in the heart tissue did not match those applied by the pressure controller.

Heart rate increased with temperature for all replicates (Figure 4.4a). However, embryo five (yellow line) increased by only five beats per minute (bpm), from 81 to 86 bpm. Conversely, embryo six increased by 30 bpm, from 115 to 145 bpm. On average, heart rate increased by 2.24±1.38 bpm (mean±SD) per °C. Heart rate ranges were distributed from 82 to 145 bpm. Max RBC velocity, as measured at the middle of the heart tube, increased with heart rate for most embryos. When embryos were pooled, cases with higher heart rates overall also displayed greater RBC velocities (Figure 4.4b).

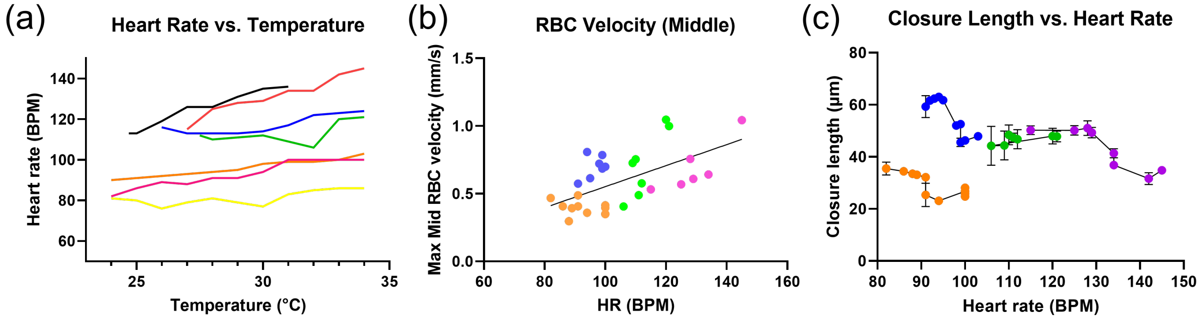

Figure 4.4: (a) Plot of heart rate vs. temperature for 24 hpf zebrafish hearts. Each colored line represents a different embryo. (b) Plot of max RBC velocity vs. heart rate. Velocity measured at the middle of 24 hpf zebrafish heart (tube). Each colored set of data points represents a different embryo. Line is a linear fit with slope of 0.002 and R^2=0.34. (c) Plot of closure length vs. heart rate for 24 hpf zebrafish (tube) hearts. Closure length measured during middle of cycle and averaged over five cycles for each temperature. Vertical lines for each data point represent standard deviations.

Closure length decreased with heart rate for most replicates but with great variation (Figure 4.4c). Three out of four embryos in which closure length was measured showed a sharp decrease in closure length and an increase in heart rate during the experiment.

Inlet RBC flow rate showed negative flows at the initiation of the cycle, indicating reverse flow (Figure 4.5a). In videos, this can be seen when the endocardial closure seems to push away RBCs in the forward and reverse directions. The zero RBC flow rate region corresponds with the period in the cycle when the closure is passing through the ROI, as such there are no RBCs in the ROI. Trailing-edge flow rate (blue line in Figure 4.5a) correlated closely with inlet RBC flow rate (black lines), however max RBC flow rate was at times up to $9*10^{-5}$ μL/s greater than or $7*10^{-5}$ μL/s less than trailing-edge flow rate. Outlet RBC flow rate is low at the start of the cycle, this is when the endocardium is beginning to close at the inlet region (Figure 4.5b). The leading-edge flow rate oscillates with a range of up to $6.3*10^{-5}$ μL/s. When outlet RBC flow rate is at its max of $26.5*10^{-5}$ μL/s, occurring at 42% cycle, leading-edge flow rate is less than half that at $12*10^{-5}$ μL/s. As the closure approaches the outlet ROI, RBC flow reduces. The closure transits the outlet ROI when there is zero flow at 54-76% cycle. The RBC flow at the end of the cycle represents the RBCs trailing the closure.

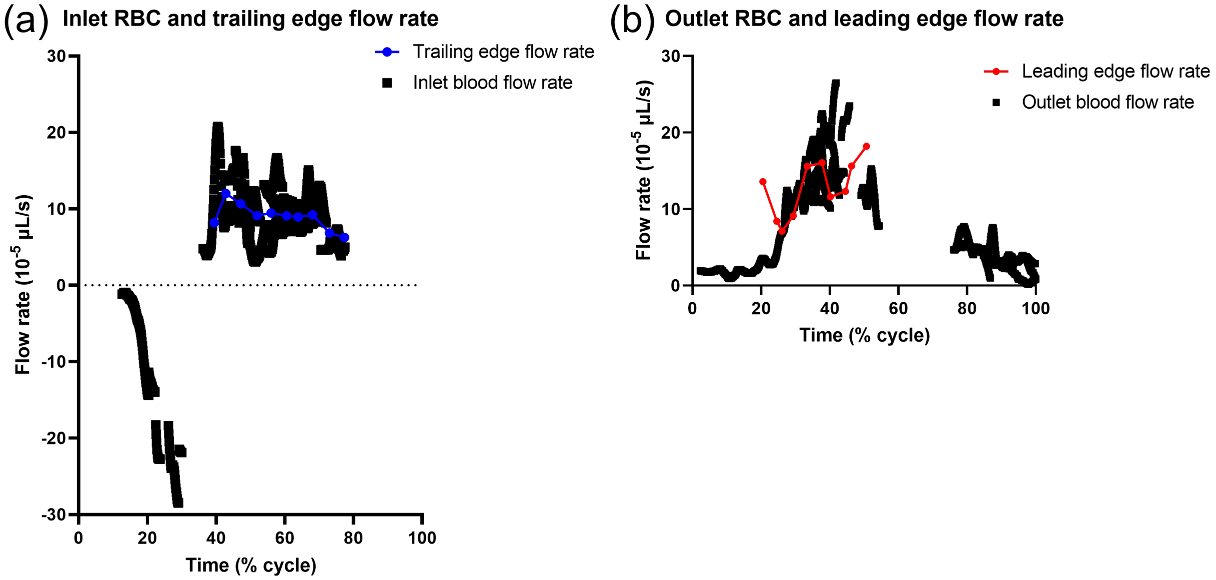

Figure 4.5: (a) Plot of inlet RBC and trailing-edge flow rate over one cycle. (b) Plot of outlet RBC and leading-edge flow rate over one cycle.

Max edge and max RBC velocities were compared in correlation plots (Figure 4.6). At the inlet, max trailing-edge and RBC velocity correlated poorly, r(29)= .20, p = .274 (Figure 4.6a). Trailing-edge and RBC velocity correlation improved at the outlet, r(29)= .37, p = .042 (Figure 4.6b). Correlation was even greater between leading-edge and inlet RBC velocity (Figure 4.6c), LE vs inlet: r(29)= .39, p = .029. However, the greatest correlation was between leading-edge and outlet RBC velocity (Figure 4.6d), LE vs outlet: r(29)= .62, p < .01. In general, leading-edge velocity correlated more closely with RBC velocity than trailing-edge velocity and outlet RBC velocities correlated more closely with edge velocity than inlet RBC velocity.

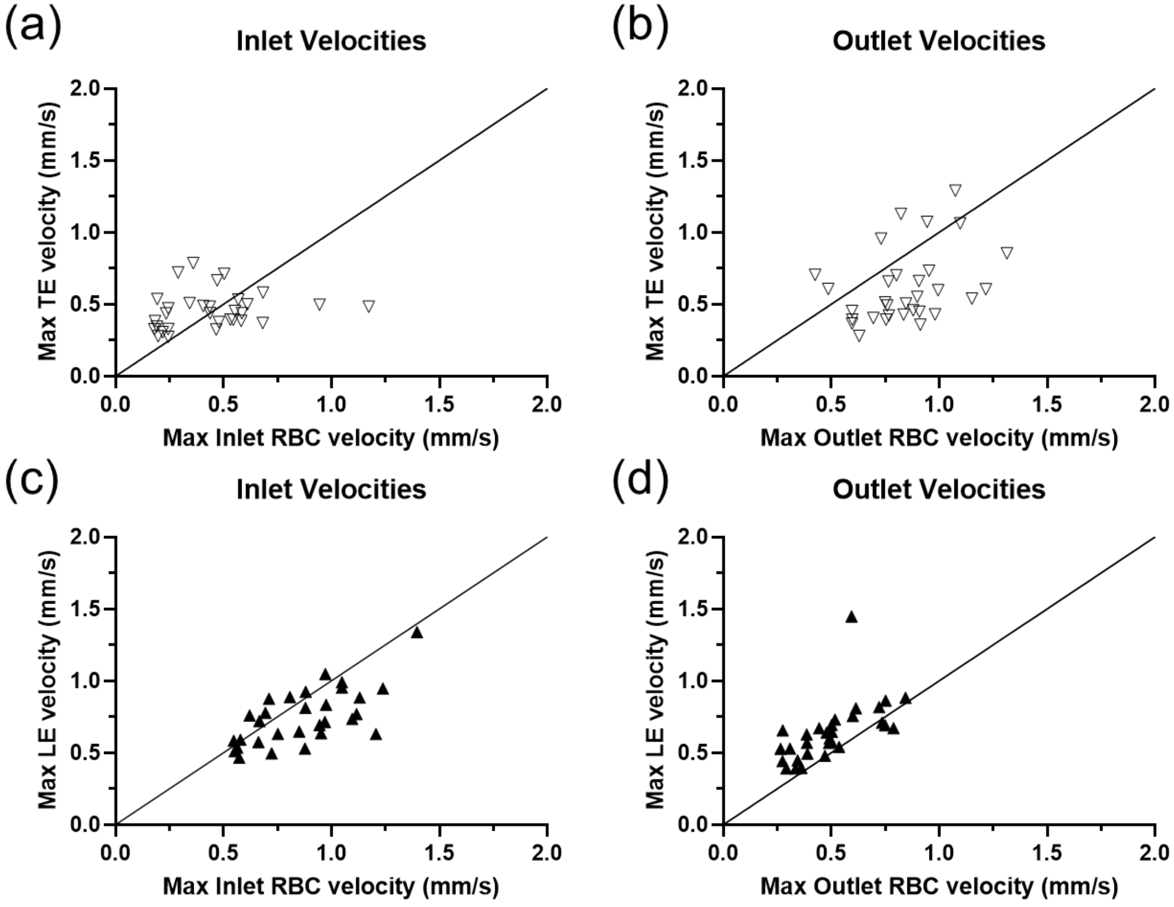

Figure 4.6: (a) Correlation plot of max trailing-edge velocity vs. max inlet RBC velocity, r(29)= .20, p = .274. (b) Correlation plot of max trailing-edge velocity vs. max outlet RBC velocity, r(29)= .37, p = .042. (c) Correlation plot of max leading-edge velocity vs. max inlet RBC velocity, r(29)= .39, p = .029. (d) Correlation plot of max leading-edge velocity vs. max outlet RBC velocity, r(29)= .62, p < .01.

4.4 Discussion

Our induced impedance pulsing technique failed to produce any forward flow. However, mismatch between applied and observed pressure pulses indicates that some pressure wave interference may be occurring. It is possible that the pressure at the tip of the cannula compared to the applied pressure is greatly reduced due to the size of the cannula inner diameter ($\sim$5 microns). Thus the pressure pulse and the effect on the surrounding fluid would be too small to generate flow. Additionally, cannula placement is technically difficult and successful impedance pump design is sensitive to positioning of the contracting region, or in our case the pulse position [7, 11]. Cannula position may have been too weak and close to the endothelial wall. Future attempts should take into account additional cannula tip sizes and cannula positioning. With that, further experimentation is needed to determine the contribution of impedance effects to embryonic tube heart flow.

Increase in temperature resulted in an increase in heart rate and max RBC velocity. For reference, 24 hpf zebrafish embryo physiological heart rate is $\sim$87-94 bpm and mean velocity ranges from 0.19-0.61 μm/s (as measured at the dorsal aorta) [12, 13]. The temperature control experiments performed here produced heart beats between 82-145 bpm, and max RBC velocity increased from 0.46 to 1.04 μm/s over a temperature range of 24 to 34 °C. This equates to a roughly 70% blood velocity increase at the highest temperature over the max measured physiological velocity. Although we did not directly measure arterial pressure, we speculate that with such a drastic blood velocity increase, cardiac output and pressure would increase as well. However, we also observed a decrease in closure length with heart rate increase for individual embryos. On average, we measured a 20% decrease from the length measured at the lowest to highest temperature. Endocardial closure length shortening appears to be a mechanism to adapt to increased heart rate, presumably from increased activity or stress. We propose two possible explanations: 1.) closure length decreases in order to increase stroke volume as cycle length gets shorter (heart rate increases) as a way to maintain the same cardiac output. If cycle length gets short enough, closure length may decrease to the point where RBCs begin leaking past the closure Or 2.) closure length decreases as arterial pressure increases. The heart is unable to generate enough contractile force to oppose this increased pressure and shortening closure length is a consequence. If arterial pressure increases enough, leakage may occur.

In similar experiments, a non-linear relationship between RBC velocity and heart rate was observed [3]. This was interpreted as the result of impedance-induced pressure wave resonance or mismatch. However, we did not observe any sharp increases or decreases in blood velocity at any particular frequency (heart rate). The drop of blood velocity observed may have occurred due to leakage across the closure as proposed above. Direct pressure measurements to evaluate impedance induced pressure increases and further investigating leakage or reverse flow across the closure would contribute more to this investigation.

In the inlet and outlet regions of the tube heart, leading-edge velocity is closely correlated with RBC velocity (Figure 4.6c and d), supporting the peristaltic pumping hypothesis that the closure displaces the blood volume at an equal rate. However, the trailing-edge velocity is poorly correlated with RBC velocity at the inlet and outlet (Figure 4.6a and b). Additionally, trailing-edge velocity is consistently lower than RBC velocity at higher heart rates. This may indicate a suction effect where a negative pressure gradient exists across the inlet, as proposed by Forouhar et al.

In summary, we find the following evidence in support of peristaltic-type (volume displacement) pumping; 1) blood flow cannot be directly induced by pressure pulses alone, 2) RBC velocity and heart rate do not have an apparent non-linear relationship, 3) Leading edge velocity is closely correlated with RBC velocity. However, we also observed potential for impedance-type pumping in the suction effect present at the closure trailing edge. Overall, it is likely that a combination of peristaltic and impedance pumping contribute to blood flow in the embryonic tube heart.

References

[1] Mark C Fishman and Kenneth R Chien. Fashioning the vertebrate heart: earliest embryonic decisions. *Development*, 124(11):2099–2117, 1997.

[2] Antoon F M Moorman, Alexandre T Soufan, Jaco Hagoort, Piet A J de Boer, and Vincent M

Christoffels. Development of the building plan of the heart. *Annals of the New York Academy of Sciences*, 1015(1):171–181, 2004.

[3] Arian S Forouhar, Michael Liebling, Anna Hickerson, Abbas Nasiraei-Moghaddam, Huai-Jen Tsai, Jay R Hove, Scott E Fraser, Mary E Dickinson, and Morteza Gharib. The embryonic vertebrate heart tube is a dynamic suction pump. *Science*, 312(5774):751–753, 2006.

[4] Niema Pahlevan and Morteza Gharib. Human Aorta Is a Passive Pump. In *APS Division of Fluid Dynamics Meeting Abstracts*, pages H16–008, 2012.

[5] Arvind Santhanakrishnan and Laura A Miller. Fluid dynamics of heart development. *Cell biochemistry and biophysics*, 61(1):1–22, 2011.

[6] Pavel Kozlovsky, Robert J Bryson-Richardson, Ariel J Jaffa, Moshe Rosenfeld, and David Elad. The Driving Mechanism for Unidirectional Blood Flow in the Tubular Embryonic Heart. *Annals of Biomedical Engineering*, 44(10):3069–3083, 2016.

[7] Alireza Sharifi, Alex Gendernalik, Deborah Garrity, and David Bark. Valveless pumping behavior of the simulated embryonic heart tube as a function of contractile patterns and myocardial stiffness. *Biomechanics and Modeling in Mechanobiology*, 20(5):2001–2012, 2021.

[8] M. Westerfield. *The Zebrafish Book*. University of Oregon Press, Eugene, OR, 1995.

[9] Dmitry Ershov, Minh-Son Phan, Joanna W Pylvänäinen, Stéphane U Rigaud, Laure Le Blanc, Arthur Charles-Orszag, James RW Conway, Romain F Laine, Nathan H Roy, Daria Bonazzi, et al. Trackmate 7: integrating state-of-the-art segmentation algorithms into tracking pipelines. *Nature methods*, 19(7):829–832, 2022.

[10] Jean-Yves Tinevez, Nick Perry, Johannes Schindelin, Genevieve M Hoopes, Gregory D Reynolds, Emmanuel Laplantine, Sebastian Y Bednarek, Spencer L Shorte, and Kevin W Eliceiri. Trackmate: An open and extensible platform for single-particle tracking. *Methods*, 115:80–90, 2017.

[11] Anna Iwaniec Hickerson, Derek Rinderknecht, and Morteza Gharib. Experimental study of the behavior of a valveless impedance pump. *Experiments in fluids*, 38:534–540, 2005.

[12] Jakob Gierten, Christian Pylatiuk, Omar T Hammouda, Christian Schock, Johannes Stegmaier, Joachim Wittbrodt, Jochen Gehrig, and Felix Loosli. Automated high-throughput heartbeat quantification in medaka and zebrafish embryos under physiological conditions. *Scientific Reports*, 10(1):2046, 2020.

[13] Jeeranan Boonruangkan, Hamid Farrokhi, Thazhe M Rohith, Samuel Kwok, Tom J Carney, Pei-Chen Su, and Young-Jin Kim. Label-free quantitative measurement of cardiovascular dynamics in a zebrafish embryo using frequency-comb-referenced-quantitative phase imaging. *Journal of Biomedical Optics*, 26(11):116004–116004, 2021.

Chapter 5

General Conclusions and Future Directions

In Aim 1, we developed a technique to cannulate and pressurize the embryonic zebrafish heart. After measuring deformation and generating pressure-stretch relationships, we attempted fits of three different constitutive models to determine material properties. Furthermore, we performed finite element analysis (FEA) to compare with experimental results and validate our findings in three-dimensions. Ultimately, we determine that the looped embryonic zebrafish heart atrium has a stiffness on the order of 10 kPa.

Residual strain is a common component of arterial mechanical properties. In this case, it is normally characterized using opening angle, whereby a cut is made laterally in the artery causing it to split open. From this, residual strain is obtained which can be used to determine residual stress. Residual strain is also used to define the actual reference configuration, in which the tissue is stress-free. In Aim 1, we neglect to measure residual strain and determine the actual stress-free reference configuration. In future experiments, we propose to use laser ablation to make an incision in the 2 dpf zebrafish heart. Two-photon laser ablation has been used to ablate structures as small as cell-cell junctions in order to measure the resulting opening angle [1]. In zebrafish, it is commonly used to ablate and disable neuronal cells [2]. With this, we can more accurately determine mechanical properties of the embryonic heart.

The pressurization technique in Aim 1 was developed using bright-field microscopy, with the reasoning that it was the most rapid and easy way to obtain images. This limited our frame of measurement to a 2D plane and thus we were unable to consider out of plane stretch. We transitioned to 3D confocal imaging in Aim 2. Although imaging speed was much slower, this allowed the technique to be used for any embryonic system that could be pressurized.

In Aim 2, we leveraged the pressurization technique to generate three-dimensional strain maps of the developing embryonic zebrafish heart. Our objective was to locate strain patterns in early stages of the heart that colocalize with structures that have not developed yet, such as trabeculae.

Furthermore, we altered the hemodynamic environment to reduce afterload pressure in the developing heart, which resulted in an overall increase in max strain compared to controls. This indicates a probable decrease in overall stiffness for embryonic hearts exposed to altered hemodynamics. This is significant in the context that altered stiffness has been correlated with congenital heart defects [3, 4]. Additionally, over-strained cardiomyocytes are prone to altered gene transcription resulting in altered contraction which may lead to further malformations [5].

In the current work, we did not detect changes in cells comprising the trabeculae at 3 dpf in *gata1* MO treated embryos vs. untreated, or for 2 vs. 3 dpf. Early trabeculae development is variable in that myocardial cardiomyocytes that are migrating into the ventricle lumen to form the trabeculae are often difficult to distinguish between non-migrating cardiomyocytes that make up the myocardial wall. However, trabeculae are less difficult to identify and quantify at 4 dpf. Additionally, we are testing a method to segment and quantify the trabecular volume based on the degree of cardiomyocyte extension passed a smooth surface delineating the myocardium. Finally, due to variability in structure development, we will increase the number of embryos that we treat and map strain on. Together, we expect these measures will allow us to connect changes in hemodynamics and strain with altered structure formation.

Although we are able to map strain and make assumptions on stiffness, we did not quantify the mechanical properties of the embryonic heart in Aim 2. Stiffness maps represent the underlying tissue architecture that ultimately defines how force is transmitted. Embryonic heart development involves a complex coordination of force transmission, as the tissue and structures are fashioned into their final forms. All the while blood flow is continually applying new mechanical signals that further inform structure development. A stiffness map provides a snapshot of current development which may be used to indicate where malformations are emerging. Furthermore, since we know hemodynamics affect development, we can use stiffness maps to determine how hemodynamics are affecting specific structures, or what magnitudes of wall shear stress or pressure the heart structures can tolerate before they begin deforming.

To that end, stiffness maps will be generated from a FEA performed on the same 3D geometry shown in our strain maps. Material constants will be obtained from Aim 1. Using a Neo-Hookean model and assuming the same stiffness for the entire heart, we will generate simulated strains. We will then generate a map that represents the difference between simulated FEA strain and actual strains shown in Aim 2. Preliminary assessments have shown that conspicuous patterns present in control ventricles at 2 dpf were not present at 3 dpf, where stiffness was more homogeneous. However, the patterns were visible in *gata1* MO treated 3 dpf. The patterns were in the same region where trabeculae form. This outcome is in agreement with published studies, where it was demonstrated that trabeculae serve to generate a more uniform stress distribution [6].

With Aim 2, we relate strain to changes in the developing heart under altered hemodynamic conditions. We propose to improve this aim by quantifying alterations to trabeculae and developing stiffness maps to further define the mechanical properties of the developing heart. In Aim 3, we seek to characterize the pumping behavior of the heart's earliest functional form, before trabeculae and looping. At this stage, the heart is a linear tube. However, there is debate on the method which the heart tube uses to pump, impedance or peristaltic, or a combination. Furthermore, the mechanical properties of the heart tube tissue may affect pressure pulse velocity and thus pumping, more so if impedance pumping is the primary mechanism. With that, we attempted to induce pure impedance pumping in heart tube.

Initial attempts at inducing impedance flows in the contraction halted tube heart failed, possibly due to low induced pressure. In future tests, we propose to use an enlarged tip to transfer a greater pressure pulse over a larger area. However, the 24 hpf zebrafish vasculature is a closed system with small, 5-10 μm diameter vessels. We expect that the travelling pressure waves required for closed system impedance pumping will dissipate early due to the viscous dominated environment [7].

Previously, we attempted to develop a 0D lumped parameter model based on the parameters measured in Aim 3. The goal of which was to simulate the output of the observed tube heart based on peristaltic assumptions (i.e. no contributions to flow rate other than volume displacement from contraction). Accurate simulation of cardiac output with only peristaltic assumptions would support the hypothesis that blood flow is driven by a purely peristaltic mechanism. However, if the simulations were unable to match the experimental output, we might assume that there were other mechanisms contributing to cardiac output that we were not considering in the 0D lumped parameter model. We recognize that the changing closure length might be part of a mechanism in which the heart increases stroke volume to compensate for a decreasing cycle length (increasing heart rate) under stress. Adding this dimension to the lumped parameter model may show that closure length adjustments contribute to cardiac output similar to proposed impedance pumping mechanisms.

Other aspects of the embryonic heart tube pumping function warrant future investigation. Using our pressurization method, we can determine the material properties of the embryonic heart tube. Specifically if there are any stiffness patterns that may affect how travelling pressure waves are transmitted through the heart tissue, such as in impedance pumping. As such, these parameters may contribute to an eventual tube heart 1D lumped parameter model. Furthermore, we can investigate potential stiffness variations between the aorta and ventricle to determine if impedance pumping is feasible.

With this work, we have determined that stiffness values in the embryonic zebrafish heart are on the order of 10 kPa, which is higher than previously reported [8]. Additionally, we developed a new methodology for mapping stiffness and strain throughout the heart. This technique may prove useful for phenotyping models with altered mechanical properties or hemodynamics. Furthermore, recent work has indicated that stiffness gradients exist elsewhere in the developing embryo [9]. Such gradients may exist in parts of the vasculature or any fluid filled organ system and could be characterized through 3D pressurization.

References

[1] Xuan Liang, Magdalene Michael, and Guillermo A Gomez. Measurement of mechanical tension at cell-cell junctions using two-photon laser ablation. *Bio-protocol*, 6(24):e2068–e2068, 2016.

[2] Georgeann S O'Brien, Sandra Rieger, Seanna M Martin, Ann M Cavanaugh, Carlos Portera-Cailliau, and Alvaro Sagasti. Two-photon axotomy and time-lapse confocal imaging in live zebrafish embryos. *JoVE (Journal of Visualized Experiments)*, (24):e1129, 2009.

[3] Madeline Midgett, Sevan Goenezen, and Sandra Rugonyi. Blood flow dynamics reflect degree of outflow tract banding in Hamburger-Hamilton stage 18 chicken embryos. *Journal of the Royal Society, Interface*, 11(100):20140643, nov 2014.

[4] Madeline Midgett and Sandra Rugonyi. Congenital heart malformations induced by hemodynamic altering surgical interventions. *Frontiers in physiology*, 5:287, aug 2014.

[5] Jeffrey G Jacot, Jody C Martin, and Darlene L Hunt. Mechanobiology of cardiomyocyte development. *Journal of biomechanics*, 43(1):93–98, 2010.

[6] Ming Yang, Larry A Taber, and Edward B Clark. A nonliner poroelastic model for the trabecular embryonic heart. 1994.

[7] Alireza Sharifi, Alex Gendernalik, Deborah Garrity, and David Bark. Valveless pumping behavior of the simulated embryonic heart tube as a function of contractile patterns and myocardial stiffness. *Biomechanics and Modeling in Mechanobiology*, 20(5):2001–2012, 2021.

[8] E A Zamir and L A Taber. Material properties and residual stress in the stage 12 chick heart during cardiac looping. *J. Biomech. Eng.*, 126, 2004.

[9] Min Zhu, Hirotaka Tao, Mohammad Samani, Mengxi Luo, Xian Wang, Sevan Hopyan, and Yu Sun. Spatial mapping of tissue properties in vivo reveals a 3d stiffness gradient in the mouse limb bud. *Proceedings of the National Academy of Sciences*, 117(9):4781–4791, 2020.